The Astronomical Journal, 161:190 (21pp), 2021 April https://doi.org/10.3847/1538-3881/abdd23

Stellar Radial Velocities in the Old Open Cluster M67 (NGC 2682). II. The Spectroscopic Binary Population

Aaron M. Geller[1,2], Robert D. Mathieu[3], David W. Latham[4], Maxwell Pollack[3], Guillermo Torres[4], and Emily M. Leiner[1,3]

[1] Center for Interdisciplinary Exploration and Research in Astrophysics (CIERA) and Department of Physics and Astronomy, Northwestern University, 1800 Sherman Avenue, Evanston, IL 60201, USA; a-geller@northwestern.edu
[2] Adler Planetarium, Department of Astronomy, 1300 South Lake Shore Drive, Chicago, IL 60605, USA
[3] Department of Astronomy, University of Wisconsin-Madison, 475 North Charter Street, Madison, WI 53706, USA
[4] Center for Astrophysics|Harvard & Smithsonian, 60 Garden Street, Cambridge, MA 02138, USA
Received 2020 November 25; accepted 2020 December 25; published 2021 March 17

Abstract

We present and analyze 120 spectroscopic binary and triple cluster members of the old (4 Gyr) open cluster M67 (NGC 2682). As a cornerstone of stellar astrophysics, M67 is a key cluster in the WIYN Open Cluster Study (WOCS); radial-velocity (RV) observations of M67 are ongoing and extend back over 45 yr, incorporating data from seven different telescopes, and allowing us to detect binaries with orbital periods $\lesssim 10^4$ days. Our sample contains 1296 stars (604 cluster members) with magnitudes of $10 \leqslant V \leqslant 16.5$ (about 1.3–0.7 $M_{\odot}$), from the giants down to ∼4 mag below the main-sequence turnoff, and extends in radius to 30′ (7.4 pc at a distance of 850 pc, or ∼7 core radii). This paper focuses primarily on the main-sequence binaries, but orbital solutions are also presented for red giants, yellow giants, and sub-subgiants. Out to our period detection limit and within our magnitude and spatial domain, we find a global main-sequence incompleteness-corrected binary fraction of $34\% \pm 3\%$, which rises to $70\% \pm 17\%$ in the cluster center. We derive a tidal circularization period of $P_{\rm circ} = 11.0^{+1.1}_{-1.0}$ days. We also analyze the incompleteness-corrected distributions of binary orbital elements and masses. The period distribution rises toward longer periods. The eccentricity distribution, beyond $P_{\rm circ}$, is consistent with a uniform distribution. The mass-ratio distribution is also consistent with a uniform distribution. Overall, these M67 binaries are closely consistent with similar binaries in the galactic field, as well as with the old (7 Gyr) open cluster NGC 188. WOCS. 83.

Unified Astronomy Thesaurus concepts: Spectroscopic binary stars (1557); Binary stars (154); Radial velocity (1332); Open star clusters (1160); Star clusters (1567); Solar analogs (1941); Catalogs (205); Observational astronomy (1145)

Supporting material: figure sets, machine-readable tables

1. Introduction

M67 (NGC 2682) is among the most well-studied open clusters. Given its old age (∼4 Gyr), proximity (∼850 pc), and low extinction ($E(B-V)$ measurements between 0.015 and 0.056), M67 serves as a powerful probe into the nature of solar-age stars near solar metallicity ([Fe/H] between +0.05 and +0.10) and into the later stages of stellar and dynamical evolution, both orbital and cluster. M67 is located at $\alpha = 8^{\rm h}51^{\rm m}23\overset{\rm s}{.}3$, $\delta = +11°49'02''$ (J2000), and is a key cluster of the WIYN Open Cluster Study (WOCS, Mathieu 2000). We refer the reader to Geller et al. (2015, hereafter, Paper I) for a thorough review of the cluster parameters and the associated literature.

M67 has been the target of radial-velocity (RV) surveys by our group and others for the past 45 yr. In Paper I we used the results from those surveys to derive improved cluster membership probabilities, to identify binaries, and to explore the kinematics of the cluster. However, we did not report the individual internal RVs in Paper I, only the average RVs known at the time or the center-of-mass RVs for binaries with orbital solutions. In this paper we report the full details of our orbital solutions for 83 single-lined binaries, 31 double-lined binaries, three triple systems with simultaneous inner and outer orbits, and an additional three candidate triple systems with only single-orbit solutions. All are high-probability cluster members. Furthermore, we include a table of all our individual RVs for nonmembers as well as members.

Binary stars influence the dynamical evolution of star clusters. Through close dynamical encounters in star clusters, energy can be exchanged between singles, binaries, and higher-order systems, and later distributed throughout the cluster via two-body relaxation processes. These close encounters, in turn, will also modify the binary population, for instance, by changing their orbital periods, eccentricities, and/or mass ratios, by inducing stellar mergers or collisions, or by fully disrupting a binary. These modifications to the birth binary population are imprinted on the binary frequency, and on distributions of orbital periods, eccentricities, and mass ratios (among others). Through long-term RV surveys, such as ours, we can begin to study these properties of the binary population in search of dynamical signatures.

The binary population is not only a tracer of cluster dynamics, but also controls the production rate and characteristics of blue stragglers (and other binary evolution products), which are thought to arise from a combination of binary mass transfer, mergers, and dynamical collisions (Leonard 1989; McCrea 1964; Perets & Fabrycky 2009; Geller & Mathieu 2011; Gosnell et al. 2015). Blue stragglers in particular have been used as probes of the accuracy of star cluster *N*-body models (e.g., Hurley et al. 2005; Geller et al. 2013), and may offer key insights into the details of the mass-transfer process.

Furthermore, *N*-body star cluster models are sophisticated enough to attempt to match very detailed observed characteristics of real star clusters, including their binaries. Hurley et al. (2005) presented an *N*-body model specifically aimed at reproducing M67, with a focus on the blue stragglers. At the time, Hurley et al. (2005) did not know the characteristics of the actual binaries in M67, and implemented common theoretical choices for initial conditions. Geller & Mathieu (2012, hereafter GM12) questioned the accuracy of the binary population in the Hurley et al. (2005) M67 model, showing that it is inconsistent with observations of another old open cluster, NGC 188. Geller et al. (2013) created an *N*-body model specifically for NGC 188, with an updated binary population to match observations, and found stark differences in the blue straggler populations between the M67 and NGC 188 models because the initial binary populations are different. Here we compare the observed M67 and NGC 188 binaries, finding close similarities between the two. Empirical studies of binary populations offer critical tests of star cluster models. In this paper, we provide a cornerstone binary population in an old open cluster to help guide such models.

M67 also contains a rich population of blue straggler stars that lie blueward of the main-sequence turnoff (Paper I). We reserve a discussion of this population of stars, including their binary orbits, for a subsequent paper.

In Section 2 we summarize our stellar sample and observations, and we provide the RV measurements in Table 1. In Section 3 we discuss our orbit-fitting procedures for both SB1s and SB2s. We present three triple stars with simultaneous solutions for the inner and outer orbits plus three additional candidate triple stars with single orbits in Section 3.3. Orbital parameters are presented in Tables 2–4, and the orbit plots are shown in Figures 1–3. In Section 4 we discuss our completeness in binary detection and orbital elements. We use a resulting completeness correction to investigate the binary frequency (Section 5) and distributions of binary orbital parameters and secondary masses (Section 6). Throughout the paper, we compare the M67 binaries to similar binaries in the galactic field (Raghavan et al. 2010, hereafter R10) and in the old (7 Gyr) open cluster NGC 188 (GM12); we synthesize this comparison in Section 7. Finally, in Section 8 we provide a summary.

2. Stellar Sample and Observations

Our database of RV measurements for M67 stars incorporates observations from seven instrument and telescope pairs (see Table 1 from Paper I), and spans a baseline of over 45 yr, allowing detection of binaries out to periods of $\sim 10^4$ days. In this section, we present a brief overview of our RV sample; a full discussion of its chronology and evolution is given in Paper I. In total, our stellar sample in M67 contains 1296 stars.

Of the 13,775 RVs used for Paper I, 42% came from the WIYN 3.5 m telescope using the Hydra multi-object spectrograph (MOS), and 55% came from CfA facilities. Over the five years since Paper I was finalized, we have continued to monitor detected velocity variables that lacked orbital solutions and also stars with uncertain membership probabilities, adding 1339 WIYN/Hydra RVs and 192 from the Tillinghast Reflector Echelle Spectrograph (TRES) to the orbital solutions and analysis presented here.

2.1. CfA Sample and Data

Our RV survey of M67 began with the dissertation work of Mathieu (1983), using the CfA Digital Speedometers (DS) on the MMT and the 1.5 m Tillinghast Reflector of the Fred Lawrence Whipple Observatory, both on Mount Hopkins, Arizona. A third DS was later commissioned at the 1.5 m Wyeth Reflector at Oak Ridge Observatory in the Town of Harvard, Massachusetts, where M67 data were also collected. Earlier RV data from the Palomar Hale 5 m observatory and the CORAVEL instrument at Haute–Provence were also added to the sample (Mathieu et al. 1986). Subsequently, observational facilities were expanded to include the TRES. Details about the observations and reduction procedures for data taken with TRES and the CfA DSs may be found in Latham (1992) and Latham et al. (2002).

2.2. WIYN Sample

Observations of M67 with the Hydra MOS on the WIYN 3.5 m began on 2005 January 15 and continue to the present day. The WIYN sample includes all stars within 30 arcmin of the cluster center, with *V*-band magnitudes in the range $10 \leqslant V \leqslant 16.5$ and with colors $(B-V)_0 > 0.4$. We note that many blue stragglers lie blueward of the color limit, but are nonetheless included in the sample due to their scientific interest. Information about the spectra and reduction procedure for WIYN data can be found in Geller et al. (2008, 2010) and Hole et al. (2009).

Additional chronological information about the sample, including date ranges, number of stars observed, and number of observations from each telescope and instrument pair, can be found in Paper I.

3. Orbit Fitting

Using our RV measurements of single- and double-lined binary systems, we fit orbital solutions to M67 RV members following the procedures outlined in Geller et al. (2009), Latham et al. (2002), and Goldberg et al. (2002). Orbital solutions were checked independently by both the WOCS and CfA groups using similar, though not identical, codes. In Table 1 we provide the heliocentric RV measurements for all stars in our database, excluding the blue straggler stars (which we will publish separately in a forthcoming paper). This table includes all the binaries with orbital solutions presented here, and also single stars, detected binaries without orbital solutions, and nonmembers. Within Table 1 we provide the WOCS ID, a cross-match ID (XID),[5] the R.A., decl., the Julian Date, the telescope and instrument pair of the observations (Tel.; "P" for Palomar Hale 5 m, "TD" for Tillinghast 1.5 m + DS, "C" for CORAVEL, "MD" for MMT + DS, "WD" for Wyeth 1.5 m + DS, "WH" for WIYN + Hydra, and "TT" for Tillinghast 1.5 m + TRES; see Paper I, and references therein, for more information on each telescope and instrument), and the heliocentric RV measurement for the primary star (RV_1), secondary star (RV_2), and tertiary star (RV_3), if relevant. For CfA RVs of single-lined stars, we provide a direct estimate of

[5] If available, the cross-reference ID is taken from Sanders (1977) and denoted by the prefix "S." If there is no Sanders (1977) match, we provide the Montgomery et al. (1993) ID, if available, denoted by the prefix "M." If both of those studies lack a match, we provide the Fan et al. (1996) IDs, if available, denoted by the prefix "F." If all of these studies lack this star, we provide the Yadav et al. (2008) ID, if available, denoted by the prefix "Y." For all sources, we also provide their R.A. and decl. positions for matching to other catalogs.

Table 1
Radial-velocity Data Table

ID	XID	R.A.	Decl.	HJD—2,400,000 (days)	Tel.	RV_1 (km s^{-1})	RV_2 (km s^{-1})	RV_3 (km s^{-1})	RV_1, e (km s^{-1})	$Correlation_1$ Height	$(O-C)_1$ (km s^{-1})	$(O-C)_2$ (km s^{-1})	$(O-C)_{1,out}$ (km s^{-1})	$(O-C)_{2,out}$ (km s^{-1})	Phase	$Phase_{out}$
1001	S1024	08:51:22.91	+11:48:49.40	…	…	…	…	…	…	…	…	…	…	…	…	…
…	…	…	…	45784.8376	TD	10.60	56.86	…	…	…	0.28	0.32	…	…	0.0645	…
…	…	…	…	45807.6793	TD	−31.66	101.01	…	…	…	2.97	−0.88	…	…	0.2549	…
…	…	…	…	46065.0463	MD	−30.25	99.10	…	…	…	0.16	1.46	…	…	0.2022	…
…	…	…	…	46072.0582	TD	−27.84	94.82	…	…	…	−1.03	0.82	…	…	0.1815	…
…	…	…	…	46125.8883	TD	93.85	−32.79	…	…	…	−2.49	−2.56	…	…	0.7002	…
…	…	…	…	46162.6236	TD	97.02	−28.00	…	…	…	2.06	0.85	…	…	0.8311	…
…	…	…	…	46393.0446	MD	29.17	35.04	…	…	…	−2.16	−0.30	…	…	0.0147	…
…	…	…	…	46423.0430	TD	−30.90	97.89	…	…	…	−0.12	−0.12	…	…	0.2047	…
…	…	…	…	46423.9877	TD	−27.12	94.08	…	…	…	−0.45	0.22	…	…	0.3367	…

(This table is available in its entirety in machine-readable form.)

Table 2
Orbital Parameters for M67 Single-lined Binaries

ID	XID	P (days)	Orbital Cycles	γ (km s^{-1})	K (km s^{-1})	e	ω (deg)	$T_\circ$ (HJD—2,400,000 days)	$a \sin i$ (10^6 km)	$f(m)$ ($M_\odot$)	σ (km s^{-1})	N
1005	S1250	4422	2.8	33.64	2.59	0.529	81	47587	133	4.8×10^{-3}	0.44	111
		±17		±0.05	±0.08	±0.023	±3	±20	±5	$\pm 0.5 \times 10^{-3}$		
1015	S1237	698.56	23.9	33.58	5.02	0.087	260	46574	48.0	9.1×10^{-3}	0.44	75
		±0.24		±0.06	±0.07	±0.015	±10	±19	±0.7	$\pm 0.4 \times 10^{-3}$		
1033	S721	6350	2.5	34.53	0.98	0.54	266	46860	71	3.6×10^{-4}	0.41	89
		±220		±0.06	±0.09	±0.07	±10	±220	±8	$\pm 1.1 \times 10^{-4}$		
2002	S1040	42.8251	382.4	33.00	8.47	0.016	80	45539	4.99	2.70×10^{-3}	0.54	60
		±0.0010		±0.07	±0.10	±0.012	±50	±5	±0.06	$\pm 0.10 \times 10^{-3}$		
2008	S1072	1513	10.8	32.70	2.57	0.30	158	46889	51	2.3×10^{-3}	1.05	71
		±7		±0.13	±0.19	±0.07	±14	±52	±4	$\pm 0.5 \times 10^{-3}$		
2014	S1221	6475	2.5	32.85	5.71	0.037	320	52500	508	1.25×10^{-1}	0.44	110
		±16		±0.05	±0.07	±0.011	±19	±300	±6	$\pm 0.05 \times 10^{-1}$		
2016	S1224W	12.4424	558.5	33.48	22.06	0.025	246	48115.7	3.77	1.38×10^{-2}	1.02	44
		±0.0005		±0.17	±0.25	±0.010	±25	±0.8	±0.04	$\pm 0.05 \times 10^{-2}$		
2017	S961	6500	2.0	33.42	3.95	0.62	276	50470	278	2.0×10^{-2}	0.68	42
		±240		±0.11	±0.22	±0.05	±5	±40	±20	$\pm 0.4 \times 10^{-2}$		
2032	S839	1651	3.7	33.2	4.1	0.37	118	50750	87	9×10^{-3}	0.95	23
		±24		±0.3	±0.4	±0.10	±16	±90	±8	$\pm 3 \times 10^{-3}$		
2041	S1397	300.418	42.5	33.85	14.7	0.837	32	49896.3	33.3	1.62×10^{-2}	1.21	40
		±0.019		±0.20	±0.7	±0.011	±3	±0.4	±1.9	$\pm 0.25 \times 10^{-2}$		
2068	S277	8540	1.2	35.51	8.3	0.859	295.0	47818	500	6.8×10^{-2}	0.90	95
		±250		±0.14	±0.3	±0.013	±2.1	±13	±30	$\pm 0.9 \times 10^{-2}$		
3001	S1031	128.14	83.0	33.4	10.3	0.04	120	49242	18.1	1.43×10^{-2}	1.55	37
		±0.03		±0.3	±0.4	±0.04	±60	±21	±0.7	$\pm 0.17 \times 10^{-2}$		
3004	S1264	353.25	37.1	33.49	11.47	0.397	83	46173.1	51.2	4.28×10^{-2}	0.56	35
		±0.08		±0.10	±0.16	±0.009	±3	±1.7	±0.7	$\pm 0.18 \times 10^{-2}$		
3014	S1285	278.2	22.3	33.76	8.1	0.18	176	46206	30.4	1.45×10^{-2}	0.97	25
		±1.1		±0.20	±0.3	±0.03	±12	±8	±1.1	$\pm 0.16 \times 10^{-2}$		
3020	S816	414.6	16.9	33.1	11.3	0.49	60	52635	56	4.1×10^{-2}	0.84	26
		±0.7		±0.7	±0.9	±0.04	±4	±11	±5	$\pm 1.0 \times 10^{-2}$		
3023	S821	583.4	4.0	33.22	10.42	0.791	191.6	47437.0	51.1	1.56×10^{-2}	0.69	44
		±0.8		±0.12	±0.22	±0.011	±1.9	±1.1	±1.6	$\pm 0.12 \times 10^{-2}$		
3063	S251	947.4	10.5	34.36	6.52	0.551	328	46733	71	1.58×10^{-2}	0.63	35
		±2.0		±0.12	±0.21	±0.020	±3	±4	±3	$\pm 0.16 \times 10^{-2}$		
4001	S1029	139.77	70.6	32.63	12.27	0.36	264	53507.2	22.0	2.17×10^{-2}	0.84	29
		±0.03		±0.23	±0.24	±0.03	±4	±1.8	±0.5	$\pm 0.13 \times 10^{-2}$		
4004	S1007	7400	1.4	34.75	3.1	0.70	260	49640	220	8×10^{-3}	0.72	58
		±300		±0.19	±0.9	±0.14	±14	±70	±80	$\pm 8 \times 10^{-3}$		
4007	S986	10.338098	1187.0	33.52	33.83	0.004	290	50167	4.809	4.15×10^{-2}	0.81	45
		±0.000020		±0.14	±0.17	±0.005	±90	±3	±0.024	$\pm 0.06 \times 10^{-2}$		
4020	S736	404.69	12.8	33.89	11.5	0.29	88	50489	61.5	5.7×10^{-2}	0.59	20
		±0.23		±0.16	±0.3	±0.03	±4	±3	±1.6	$\pm 0.4 \times 10^{-2}$		
4021	S815	6166	1.9	34.46	7	0.83	14	54339	340	4×10^{-2}	0.83	82
		±21		±0.16	±4	±0.07	±5	±18	±190	$\pm 7 \times 10^{-2}$		
4034	S1612	9.10752	445.7	33.53	16.90	0.007	250	55537.6	2.117	4.55×10^{-3}	0.63	33
		±0.00012		±0.13	±0.20	±0.010	±90	±2.3	±0.024	$\pm 0.16 \times 10^{-3}$		
4039	S711	5.65093	1296.6	33.08	15.91	0.011	360	49258.5	1.236	2.36×10^{-3}	0.99	42
		±0.00010		±0.16	±0.21	±0.014	±70	±1.2	±0.017	$\pm 0.10 \times 10^{-3}$		
4051	S1808	10610	1.2	32.75	4.12	0.713	283	57540	421	2.6×10^{-2}	0.61	84
		±120		±0.10	±0.14	±0.014	±3	±25	±16	$\pm 0.3 \times 10^{-2}$		
5008	S1275	14800	0.9	34.03	4.7	0.47	18	50710	850	1.1×10^{-1}	0.44	73
		±800		±0.22	±0.4	±0.04	±5	±220	±80	$\pm 0.3 \times 10^{-1}$		
5009	S1076	4600	2.5	34.33	1.65	0.21	122	53390	102	2.0×10^{-3}	0.34	57
		±110		±0.07	±0.09	±0.04	±14	±220	±6	$\pm 0.3 \times 10^{-3}$		
5018	S740	14.55331	278.6	34.55	14.42	0.258	150.3	55515.31	2.788	4.08×10^{-3}	0.35	32
		±0.00015		±0.07	±0.09	±0.006	±1.4	±0.05	±0.018	$\pm 0.08 \times 10^{-3}$		
5030	S1586	141.27	49.2	32.76	5.7	0.23	198	53562	10.8	2.5×10^{-3}	0.88	31
		±0.06		±0.16	±0.3	±0.04	±12	±5	±0.6	$\pm 0.4 \times 10^{-3}$		
5037	S1508	25.868	82.0	33.47	20.9	0.437	318.7	46569.08	6.69	1.78×10^{-2}	0.69	26
		±0.003		±0.15	±0.3	±0.008	±1.6	±0.08	±0.10	$\pm 0.07 \times 10^{-2}$		
5045	S1634	3250	1.9	32.9	5.5	0.50	284	51750	214	3.7×10^{-2}	1.06	22
		±90		±0.3	±0.4	±0.05	±12	±130	±19	$\pm 0.9 \times 10^{-2}$		

Table 2
(Continued)

ID	XID	P (days)	Orbital Cycles	γ (km s^{-1})	K (km s^{-1})	e	ω (deg)	$T_\circ$ (HJD—2,400,000 days)	$a \sin i$ (10^6 km)	$f(m)$ ($M_\odot$)	σ (km s^{-1})	N
5049	S905	16.8338 ±0.0006	438.6	34.39 ±0.21	14.5 ±0.3	0.060 ±0.020	61 ±19	50715.7 ±0.9	3.35 ±0.06	5.3×10^{-3} $\pm 0.3 \times 10^{-3}$	1.11	35
6003	S1012	643 ±3	4.0	35.7 ±0.3	7.8 ±0.4	0.26 ±0.04	212 ±11	47780 ±19	67 ±4	2.8×10^{-2} $\pm 0.5 \times 10^{-2}$	0.92	17
6008	S1242	31.7774 ±0.0006	449.3	33.80 ±0.12	10.3 ±0.3	0.657 ±0.013	146.0 ±1.9	48193.05 ±0.07	3.41 ±0.11	1.56×10^{-3} $\pm 0.13 \times 10^{-3}$	0.78	44
6016	S760	960 ±6	6.4	33.2 ±0.3	8.2 ±0.8	0.46 ±0.08	223 ±7	50906 ±13	97 ±10	3.9×10^{-2} $\pm 1.2 \times 10^{-2}$	1.20	23
6017	S1320	38.763 ±0.004	39.1	33.93 ±0.12	24.3 ±0.5	0.506 ±0.015	139.6 ±0.9	54351.19 ±0.08	11.2 ±0.3	3.71×10^{-2} $\pm 0.25 \times 10^{-2}$	0.44	18
6026	S939	105.70 ±0.03	20.5	32.54 ±0.09	12.52 ±0.11	0.124 ±0.010	73 ±3	49782.1 ±1.0	18.06 ±0.16	2.10×10^{-2} $\pm 0.05 \times 10^{-2}$	0.29	17
7004	S1000	529.9 ±1.0	12.6	33.78 ±0.17	9.84 ±0.22	0.103 ±0.023	177 ±14	46274 ±20	71.3 ±1.6	5.1×10^{-2} $\pm 0.3 \times 10^{-2}$	0.88	34
7022	S745	9.12707 ±0.00010	802.3	34.30 ±0.18	19.86 ±0.25	0.028 ±0.013	14 ±24	49184.3 ±0.6	2.49 ±0.03	7.4×10^{-3} $\pm 0.3 \times 10^{-3}$	1.21	52
8002	S2216	266.73 ±0.11	41.5	33.40 ±0.13	9.87 ±0.20	0.436 ±0.021	346 ±3	53441.4 ±1.7	32.6 ±0.8	1.93×10^{-2} $\pm 0.13 \times 10^{-2}$	0.67	32
8007	S1017	2580 ±80	2.8	35.2 ±0.4	4.2 ±0.4	0.21 ±0.14	190 ±30	49900 ±200	146 ±13	1.9×10^{-2} $\pm 0.5 \times 10^{-2}$	1.11	19
8028	S1487	8675 ±12	1.5	33.19 ±0.05	6.03 ±0.11	0.746 ±0.009	285.8 ±1.5	57823 ±7	479 ±11	5.8×10^{-2} $\pm 0.3 \times 10^{-2}$	0.43	95
8046	S913	63.115 ±0.008	64.3	33.55 ±0.11	7.56 ±0.21	0.191 ±0.020	152 ±7	55558.2 ±1.1	6.44 ±0.18	2.67×10^{-3} $\pm 0.22 \times 10^{-3}$	0.54	31
8054	S1838	11.190112 ±0.00016	361.2	33.9 ±0.3	45.0 ±0.4	0.024 ±0.008	165 ±18	55839.6 ±0.6	6.92 ±0.06	1.05×10^{-1} $\pm 0.03 \times 10^{-1}$	0.97	18
9005	S1005	2769 ±18	4.2	32.91 ±0.16	5.1 ±0.3	0.15 ±0.05	177 ±17	48070 ±130	192 ±11	3.7×10^{-2} $\pm 0.6 \times 10^{-2}$	0.89	33
9011	S773	5.781069 ±0.000021	1263.8	35.18 ±0.23	54.1 ±0.3	0.006 ±0.006	100 ±60	49220.0 ±1.0	4.30 ±0.03	9.51×10^{-2} $\pm 0.17 \times 10^{-2}$	1.53	45
9012	S1300	82.8807 ±0.0013	48.9	34.17 ±0.08	18.4 ±0.3	0.767 ±0.004	64.3 ±1.0	55703.32 ±0.06	13.46 ±0.22	1.42×10^{-2} $\pm 0.06 \times 10^{-2}$	0.38	33
10013	S1249	53.016 ±0.011	97.6	32.68 ±0.22	19.6 ±0.4	0.229 ±0.016	26 ±4	54571.7 ±0.7	13.9 ±0.3	3.83×10^{-2} $\pm 0.23 \times 10^{-2}$	0.87	23
11004	S1046	907 ±5	8.4	33.5 ±0.3	7.2 ±0.3	0.11 ±0.07	320 ±30	49200 ±70	89 ±4	3.4×10^{-2} $\pm 0.5 \times 10^{-2}$	0.95	20
11010	S973	40.408 ±0.003	81.0	35.63 ±0.17	14.91 ±0.24	0.209 ±0.014	107 ±5	47947.9 ±0.5	8.10 ±0.14	1.30×10^{-2} $\pm 0.06 \times 10^{-2}$	0.79	25
11022	S1109	1060 ±3	3.8	33.17 ±0.14	7.68 ±0.21	0.402 ±0.021	87 ±5	56016 ±10	102 ±3	3.8×10^{-2} $\pm 0.3 \times 10^{-2}$	0.69	34
11025	S621	58.809 ±0.005	69.0	32.77 ±0.17	19.7 ±0.3	0.186 ±0.014	260 ±3	55248.7 ±0.5	15.66 ±0.24	4.42×10^{-2} $\pm 0.20 \times 10^{-2}$	0.70	28
11044	S650	903 ±3	4.5	35.22 ±0.17	10.4 ±0.4	0.881 ±0.008	279 ±5	55482.4 ±2.4	61 ±3	1.11×10^{-2} $\pm 0.13 \times 10^{-2}$	0.80	34
11055	S868	275.72 ±0.18	14.7	33.78 ±0.10	7.98 ±0.13	0.168 ±0.015	229 ±6	55481 ±5	29.8 ±0.5	1.39×10^{-2} $\pm 0.07 \times 10^{-2}$	0.48	29
12004	S1009	5.9530 ±0.0003	138.9	33.4 ±0.3	27.2 ±0.3	0.018 ±0.014	330 ±40	47560.2 ±0.7	2.22 ±0.03	1.23×10^{-2} $\pm 0.04 \times 10^{-2}$	1.17	25
12010	S990	41.868 ±0.024	228.7	33.56 ±0.24	17.7 ±0.4	0.348 ±0.017	207 ±4	47832.4 ±0.3	9.53 ±0.21	1.97×10^{-2} $\pm 0.12 \times 10^{-2}$	1.10	28
12014	S963	90.31 ±0.04	21.0	34.35 ±0.21	22.8 ±0.3	0.563 ±0.011	59.4 ±1.3	47710.3 ±0.4	23.4 ±0.4	6.3×10^{-2} $\pm 0.3 \times 10^{-2}$	0.72	23
12020	S1102	757.5 ±2.3	6.8	33.95 ±0.23	7.23 ±0.20	0.07 ±0.03	170 ±40	55500 ±80	75.1 ±2.1	2.95×10^{-2} $\pm 0.25 \times 10^{-2}$	0.83	38
12021	S1107	2970 ±70	1.7	34.43 ±0.16	2.90 ±0.24	0.06 ±0.08	130 ±70	54000 ±600	118 ±10	7.5×10^{-3} $\pm 1.8 \times 10^{-3}$	0.94	40
12022	S1331	161.66 ±0.03	25.1	34.56 ±0.15	20.9 ±0.4	0.522 ±0.011	44.3 ±1.3	55401.9 ±0.4	39.6 ±0.8	9.4×10^{-2} $\pm 0.5 \times 10^{-2}$	0.78	32
13004	S1011	14620 ±800	0.8	33.03 ±0.27	7.50 ±0.22	0.14 ±0.05	85 ±14	46260 ±440	1492 ±46	6.2×10^{-1} $\pm 0.7 \times 10^{-1}$	0.60	60
13008	S1063	18.38775 ±0.00009	878.7	34.55 ±0.13	19.87 ±0.20	0.207 ±0.009	97.9 ±2.9	50718.60 ±0.13	4.91 ±0.05	1.40×10^{-2} $\pm 0.04 \times 10^{-2}$	0.85	45

Table 2
(Continued)

ID	XID	P (days)	Orbital Cycles	γ (km s^{-1})	K (km s^{-1})	e	ω (deg)	$T_\circ$ (HJD—2,400,000 days)	$a \sin i$ (10^6 km)	$f(m)$ ($M_\odot$)	σ (km s^{-1})	N
13019	S810	10.15305 ±0.00008	1012.9	34.4 ±0.3	22.8 ±0.5	0.023 ±0.020	220 ±50	50413.1 ±1.4	3.18 ±0.07	1.25×10^{-2} $\pm 0.08 \times 10^{-2}$	1.89	37
13022	S2227	66.827 ±0.007	65.8	34.52 ±0.10	10.35 ±0.15	0.224 ±0.015	294 ±3	55961.4 ±0.6	9.23 ±0.14	7.0×10^{-3} $\pm 0.3 \times 10^{-3}$	0.42	22
14007	S1070	2.660606 ±0.000001	4112.2	34.02 ±0.17	68.28 ±0.23	0.006 ±0.003	220 ±40	53636.3 ±0.3	2.498 ±0.008	8.77×10^{-2} $\pm 0.08 \times 10^{-2}$	1.55	89
14020	S1452	358.9 ±0.7	28.5	32.8 ±0.3	4.1 ±0.3	0.23 ±0.07	331 ±17	54769 ±20	19.7 ±1.4	2.4×10^{-3} $\pm 0.5 \times 10^{-3}$	0.67	32
14023	S942	225.57 ±0.07	23.0	33.64 ±0.13	7.8 ±0.3	0.588 ±0.021	262 ±4	55638.0 ±1.0	19.5 ±0.8	5.8×10^{-3} $\pm 0.6 \times 10^{-3}$	0.78	39
15022	S1201	4640 ±90	1.1	34.29 ±0.06	5.30 ±0.11	0.419 ±0.018	25.3 ±2.7	55370 ±30	306 ±7	5.3×10^{-2} $\pm 0.4 \times 10^{-2}$	0.37	44
16006	S1064	777.4 ±1.0	9.4	32.53 ±0.16	6.3 ±0.7	0.73 ±0.03	34 ±8	51135 ±5	46 ±5	6.4×10^{-3} $\pm 2.1 \times 10^{-3}$	0.67	23
16020	S951	2808 ±22	2.6	33.93 ±0.16	4.52 ±0.22	0.50 ±0.04	268 ±8	50740 ±50	151 ±8	1.8×10^{-2} $\pm 0.3 \times 10^{-2}$	0.49	13
16025	S1329	5.32187 ±0.00003	882.6	33.7 ±0.3	43.4 ±0.4	0.005 ±0.008	230 ±120	56443.7 ±1.7	3.17 ±0.03	4.50×10^{-2} $\pm 0.12 \times 10^{-2}$	0.84	18
17004	S1050	3.300909 ±0.000014	5223.8	33.77 ±0.13	5.70 ±0.16	0.024 ±0.031	200 ±70	53267.8 ±0.7	0.259 ±0.007	6.3×10^{-5} $\pm 0.5 \times 10^{-5}$	0.86	52
17007	S982	373.6 ±0.8	31.5	33.3 ±0.3	4.2 ±0.3	0.26 ±0.07	199 ±17	49765 ±15	21.1 ±1.6	2.7×10^{-3} $\pm 0.6 \times 10^{-3}$	0.97	33
18006	S1065	149.64 ±0.21	12.3	34.7 ±0.3	17.7 ±0.4	0.08 ±0.03	117 ±13	47825 ±6	36.3 ±0.7	8.5×10^{-2} $\pm 0.5 \times 10^{-2}$	0.97	16
19026	S1193	2740 ±60	1.7	33.42 ±0.15	3.3 ±0.6	0.55 ±0.09	148 ±8	54020 ±60	104 ±19	6×10^{-3} $\pm 3 \times 10^{-3}$	0.65	23
20007	S2222	25.672 ±0.008	40.6	34.92 ±0.24	30.9 ±0.4	0.551 ±0.011	68.4 ±1.6	47545.06 ±0.06	9.10 ±0.14	4.6×10^{-2} $\pm 0.19 \times 10^{-2}$	1.04	20
21004	S1253	134.22 ±0.03	33.5	32.76 ±0.14	23.0 ±0.3	0.501 ±0.010	256.6 ±1.2	55985.4 ±0.4	36.8 ±0.5	1.10×10^{-1} $\pm 0.05 \times 10^{-1}$	0.37	12
21022	S1442	96.800 ±0.013	41.9	32.20 ±0.12	16.68 ±0.18	0.046 ±0.011	159 ±14	55596 ±4	22.17 ±0.24	4.63×10^{-2} $\pm 0.15 \times 10^{-2}$	0.58	27
22007	S1002	699.1 ±1.2	15.5	33.8 ±0.3	6.5 ±0.3	0.26 ±0.05	141 ±13	54082 ±24	61 ±3	1.8×10^{-2} $\pm 0.3 \times 10^{-2}$	1.15	31
23007	S1297	12.0746 ±0.0008	237.7	33.6 ±0.4	25.0 ±0.5	0.010 ±0.019	280 ±140	48061 ±5	4.15 ±0.09	1.2×10^{-2} $\pm 0.12 \times 10^{-2}$	1.27	15
23022	S943	31.0097 ±0.0019	86.6	33.30 ±0.21	22.2 ±0.4	0.391 ±0.011	206.8 ±2.4	55207.21 ±0.18	8.70 ±0.15	2.7×10^{-2} $\pm 0.13 \times 10^{-2}$	1.12	36
23023	S613	147.28 ±0.03	35.2	34.64 ±0.24	17.7 ±0.5	0.183 ±0.017	237 ±6	56412.3 ±2.4	35.2 ±0.9	8.0×10^{-2} $\pm 0.6 \times 10^{-2}$	0.64	19
25005	M5878	11.4058 ±0.0007	383.6	33.9 ±1.4	36.7 ±1.9	0.16 ±0.04	177 ±16	55587.0 ±0.5	5.7 ±0.3	5.6×10^{-2} $\pm 0.9 \times 10^{-2}$	3.17	13

(This table is available in machine-readable form.)

the uncertainty on the primary RV ($RV_{1,e}$; Kurtz & Mink 1998). For WIYN RVs of single-lined stars, we provide the cross-correlation peak height for the primary star as an indicator of the uncertainty on the RV measurement (see Geller et al. 2008, 2010). For binaries with orbital solutions, we provide the residuals for the primary star from the orbital solution fit ($(O-C)_1$). If the orbital solution is double lined, we also provide the secondary residuals from the orbital solution ($(O-C)_2$). For triple systems that have a solution to the outer orbit, we provide the residuals from this outer orbit as $(O-C)_{1,\rm out}$ and $(O-C)_{2,\rm out}$ (and see Section 3.3 for further details). Finally, for binaries with orbits we provide the phase of the observation ("Phase"), and for triples with outer orbits we also provide the phase related to the outer orbit ("$\rm Phase_{out}$"). Only a portion of the table is shown in this paper; the entire table is available online in machine-readable format. Summary information for these stars (their photometry, membership, and binarity status, etc.) is available in Table 2 of Paper I.

Membership is assessed using the center-of-mass γ-velocity of the system within the formalism, and using the same membership criteria as in Paper I. Only orbits of M67 binaries that are both RV and proper-motion members are presented. A subset of these binaries was previously presented in Mathieu et al. (1990). We confirm all those orbital solutions with our expanded data set. For two of the Mathieu et al. (1990) SB1s, we now detect the secondary spectra and derive SB2 orbits (WOCS IDs 3015 and 6010).

For an orbital solution to be secure, the phased RV measurements clearly follow the visual trend of the orbit curve, relative errors on orbital parameters are low, and root mean square (rms) residuals (σ) are near the RV measurement precision (0.5 km s^{-1} overall for WIYN; see Paper I for more

Table 3
Orbital Parameters for M67 Double-lined Binaries

ID	XID	P (days)	Orbital Cycles	γ (km s^{-1})	K (km s^{-1})	e	ω (deg)	$T_\circ$ (HJD—2,400,000 days)	$a \sin i$ (10^6 km)	$m \sin^3 i$ ($M_\odot$)	q	σ (km s^{-1})	N
1001	S1024	7.15957	242.3	33.33	68.0	0.005	90	46593.4	6.70	0.950	0.992	1.41	34
		±0.00007		±0.17	±0.3	±0.004	±40	±0.8	±0.03	±0.011	±0.007		
					68.6				6.75	0.942		1.46	34
					±0.3				±0.04	±0.011			
2003	S1045	7.64528	243.8	34.13	63.4	0.008	340	46322.8	6.66	0.818	0.993	1.76	37
		±0.00008		±0.20	±0.4	±0.004	±30	±0.7	±0.04	±0.012	±0.009		
					63.8				6.71	0.812		1.69	37
					±0.4				±0.04	±0.012			
3002	S1018	200.89	7.1	33.38	22.1	0.294	246	47689.3	58.3	0.90	0.933	1.06	32
		±0.17		±0.16	±0.3	±0.010	±3	±1.3	±0.9	±0.04	±0.024		
					23.7				62.6	0.84		1.57	32
					±0.5				±1.3	±0.03			
3006	S1053	123.45	23.7	34.28	18.28	0.465	147.9	46319.5	27.5	0.300	0.853	1.09	52
		±0.03		±0.14	±0.24	±0.010	±1.5	±0.3	±0.4	±0.013	±0.017		
					21.4				32.2	0.256		1.73	52
					±0.4				±0.6	±0.009			
3015	S1216	60.445	29.3	33.07	27.51	0.453	334.3	46641.29	20.39	1.05	0.61	0.62	33
		±0.005		±0.12	±0.19	±0.006	±0.8	±0.10	±0.14	±0.13	±0.03		
					45.1				33.4	0.64		8.55	33
					±2.4				±1.8	±0.05			
4016	S1224E	1046.3	6.9	34.68	13.4	0.340	190	48678	182	0.82	1.03	1.44	33
		±1.8		±0.19	±0.3	±0.023	±4	±9	±5	±0.05	±0.04		
					13.1				177	0.85		1.61	33
					±0.4				±5	±0.05			
5041	S1624	30.443	47.3	33.10	40.3	0.225	337.1	49627.64	16.45	1.19	0.807	1.00	15
		±0.004		±0.24	±0.5	±0.009	±2.2	±0.18	±0.21	±0.05	±0.019		
					50.0				20.4	0.96		2.08	13
					±0.9				±0.4	±0.03			
6002	S1014	16.2195	74.9	33.70	41.9	0.304	162.2	47484.77	8.89	0.65	0.812	1.24	31
		±0.0010		±0.21	±0.4	±0.007	±1.4	±0.06	±0.08	±0.03	±0.017		
					51.5				10.95	0.530		3.17	31
					±0.9				±0.21	±0.014			
6005	S999	10.05560	824.3	34.66	51.7	0.007	330	46102.1	7.15	0.755	0.875	1.84	45
		±0.00009		±0.18	±0.4	±0.005	±30	±1.0	±0.06	±0.010	±0.008		
					59.1				8.17	0.661		1.51	45
					±0.3				±0.05	±0.011			
6010	S1272	11.02146	169.3	33.06	54.7	0.258	190.4	46361.34	8.01	1.22	0.751	1.03	30
		±0.00012		±0.22	±0.3	±0.005	±1.1	±0.03	±0.05	±0.05	±0.015		
					72.8				10.66	0.915		5.29	30
					±1.3				±0.21	±0.022			
6029	S929	151.475	10.3	32.78	25.58	0.433	261.5	55603.83	48.01	0.996	0.881	0.38	25
		±0.022		±0.07	±0.10	±0.003	±0.6	±0.16	±0.20	±0.015	±0.007		
					29.05				54.5	0.877		0.70	25
					±0.18				±0.4	±0.011			
6075	S1962	156.18	22.8	33.16	20.9	0.326	174.8	50503.5	42.4	0.51	0.99	1.09	20
		±0.05		±0.19	±0.4	±0.014	±2.3	±1.0	±1.0	±0.03	±0.03		
					21.2				43.0	0.51		1.26	20

Table 3
(Continued)

ID	XID	P (days)	Orbital Cycles	γ (km s^{-1})	K (km s^{-1})	e	ω (deg)	$T_\circ$ (HJD—2,400,000 days)	$a \sin i$ (10^6 km)	$m \sin^3 i$ ($M_\odot$)	q	σ (km s^{-1})	N
					±0.5				±1.1	±0.03			
7002	S1019	1.36016	846.2	33.8	25.5	0.01	30	47828.21	0.476	0.013	0.84	1.45	22
		±0.00003		±0.3	±0.4	±0.016	±200	±0.44	±0.009	±0.001	±0.03		
					30.4				0.568	0.0112		3.37	22
					±1.0				±0.020	±0.0006			
7011	S1308	236.5	10.4	32.9	21.7	0.391	123	49258.6	64.8	1.05	0.86	1.37	24
		±0.3		±0.3	±0.7	±0.022	±3	±1.9	±1.9	±0.15	±0.05		
					25.2				75	0.91		3.75	24
					±1.5				±5	±0.09			
7016	S1457	115.89	21.6	33.76	17.4	0.417	139	48513.7	25.2	0.205	0.96	0.89	18
		±0.07		±0.21	±0.4	±0.020	±3	±0.8	±0.6	±0.020	±0.05		
					18.1				26.2	0.197		2.05	18
					±0.8				±1.2	±0.014			
8013	S1314	119.701	28.2	35.00	21.60	0.336	208.1	55500.0	33.49	0.618	0.826	0.42	22
		±0.013		±0.09	±0.14	±0.006	±1.2	±0.3	±0.20	±0.015	±0.010		
					26.2				40.6	0.511		1.02	22
					±0.3				±0.5	±0.009			
9004	S2209a	165.30	33.4	33.79	22.4	0.410	203.9	50657.6	46.4	0.63	0.96	0.56	23
		±0.03		±0.12	±0.3	±0.008	±1.3	±0.5	±0.5	±0.04	±0.03		
					23.3				48.3	0.61		2.20	21
					±0.7				±1.6	±0.03			
9014	S758	112.719	16.7	35.00	26.8	0.553	352.0	48404.93	34.6	0.644	0.900	0.62	24
		±0.023		±0.13	±0.3	±0.007	±0.9	±0.19	±0.3	±0.024	±0.017		
					29.8				38.5	0.579		1.45	24
					±0.5				±0.7	±0.016			
9016	S748	623.8	13.9	33.62	20.6	0.731	157.6	51892.4	121	0.94	0.878	0.81	20
		±0.3		±0.19	±0.5	±0.007	±1.7	±2.5	±3	±0.08	±0.022		
					23.5				138	0.82		1.64	20
					±0.8				±5	±0.06			
9022	S1428	10.9675	96.4	33.80	35.49	0.002	260	49175	5.35	0.346	0.773	0.55	16
		±0.0003		±0.14	±0.22	±0.006	±170	±5	±0.04	±0.015	±0.016		
					45.9				6.92	0.267		2.26	16
					±0.8				±0.14	±0.007			
10008	S1292	100.34	12.1	34.44	27.6	0.052	210	47481.6	38.1	1.10	0.892	1.05	31
		±0.04		±0.16	±0.3	±0.008	±9	±2.5	±0.4	±0.03	±0.015		
					31.0				42.7	0.982		1.55	31
					±0.4				±0.6	±0.024			
11014	S747	6.311407	290.3	34.42	26.77	0.0038	300	55239.2	2.323	0.0689	0.856	0.21	21
		±0.000025		±0.04	±0.07	±0.0020	±50	±0.9	±0.006	±0.0007	±0.005		
					31.28				2.715	0.0590		0.50	21
					±0.15				±0.013	±0.0005			
11028	S617	62.593	41.1	32.91	38.1	0.625	235.8	49478.69	25.62	1.21	0.758	0.82	28
		±0.003		±0.17	±0.3	±0.005	±0.8	±0.07	±0.17	±0.07	±0.022		
					50.3				33.8	0.92		4.66	26
					±1.4				±1.0	±0.03			
12009	S1247	69.7269	151.2	33.39	25.74	0.064	136	47565.8	24.63	1.06	0.692	0.59	39
		±0.0012		±0.10	±0.12	±0.006	±4	±0.8	±0.12	±0.03	±0.009		

Table 3
(Continued)

ID	XID	P (days)	Orbital Cycles	γ (km s^{-1})	K (km s^{-1})	e	ω (deg)	$T_\circ$ (HJD—2,400,000 days)	$a \sin i$ (10^6 km)	$m \sin^3 i$ ($M_\odot$)	q	σ (km s^{-1})	N
					37.2				35.6	0.732		1.63	18
					±0.4				±0.4	±0.012			
13030	S625	27.0885	148.3	33.26	35.96	0.033	85	55019.5	13.39	0.568	0.958	0.56	25
		±0.0005		±0.08	±0.15	±0.003	±6	±0.5	±0.06	±0.006	±0.005		
					37.54				13.98	0.544		0.59	25
					±0.16				±0.06	±0.005			
14011	S789	96.809	41.9	34.00	14.67	0.230	150	55675.8	19.01	0.270	0.671	0.75	35
		±0.017		±0.13	±0.20	±0.013	±3	±0.8	±0.28	±0.025	±0.028		
					21.9				28.3	0.181		2.19	7
					±0.9				±1.2	±0.011			
14015	S1208	19.8548	128.5	33.68	43.6	0.135	144	47974.24	11.79	0.75	0.938	1.17	23
		±0.0006		±0.23	±0.5	±0.007	±4	±0.20	±0.13	±0.03	±0.019		
					46.4				12.56	0.707		1.86	23
					±0.7				±0.20	±0.019			
15008	S981	55.967	40.2	33.62	19.6	0.415	249.2	47585.28	13.71	0.185	0.85	1.06	29
		±0.020		±0.18	±0.3	±0.013	±2.0	±0.24	±0.23	±0.010	±0.03		
					23.1				16.2	0.156		1.86	29
					±0.5				±0.4	±0.007			
15028	S1113	2.823070	3494.8	33.7	61.0	0.022	310	48913.16	2.37	0.536	0.713	4.46	23
		±0.000005		±0.6	±1.2	±0.012	±30	±0.20	±0.05	±0.015	±0.016		
					85.5				3.32	0.383		3.06	23
					±0.8				±0.03	±0.015			
21006	S996	6.67347	284.7	34.44	65.8	0.200	125.7	47822.12	5.92	0.860	0.930	1.18	19
		±0.00007		±0.21	±0.4	±0.004	±1.4	±0.03	±0.04	±0.014	±0.009		
					70.8				6.37	0.800		1.37	19
					±0.5				±0.05	±0.013			
24021	S819	3.598520	485.7	33.39	73.55	0.001	310	57435.8	3.640	0.576	1.015	0.48	12
		±0.000010		±0.13	±0.22	±0.003	±160	±1.6	±0.014	±0.007	±0.006		
					72.5				3.586	0.585		0.91	12
					±0.4				±0.021	±0.006			

(This table is available in machine-readable form.)

Table 4
Orbital Parameters for M67 Triples

ID	XID	P (days)	Orbital Cycles	γ (km s^{-1})	K (km s^{-1})	e	ω (deg)	$T_\circ$ (HJD—2,400,000 days)	$a \sin i$ (10^6 km)	$f(m)$ ($M_\odot$)	$m \sin^3 i$ ($M_\odot$)	q	σ (km s^{-1})	N
3012	S1077													
	inner	1.3587758	8679.8	33.45	48.3	0.015	330	52100.29	0.902		0.112	0.76	3.64	99
		±0.0000007		±0.21	±0.5	±0.011	±40	±0.16	±0.010		±0.014	±0.05		
					64				1.19		0.085		11.60	16
					±4				±0.07		±0.006			
	outer	3613	3.3	33.45	6.0	0.33	233	47150	280		1.30	0.49	3.64	99
		±13		±0.21	±0.6	±0.03	±5	±57	±26		±0.14	±0.04		
					12.3				577		0.64		2.13	99
					±0.5				±20		±0.11			
4008	S2206													
	inner	18.3768	449.8	31.3	12.3	0.12	100	47955.9	3.08	3.5×10^{-3}			3.91	91
		±0.0012		±0.4	±0.6	±0.05	±23	±1.1	±0.16	$\pm 0.5 \times 10^{-3}$				
4030	S1416													
	inner	8.9918	233.1	33.4	39.4	0.333	162.5	49770.39	4.59	4.77×10^{-2}			0.92	21
		±0.0003		±0.3	±0.7	±0.014	±1.6	±0.03	±0.07	$\pm 0.22 \times 10^{-2}$				
	outer	673	3.1	33.4	7.0	0.42	75	49837	58	1.8×10^{-2}			0.92	21
		±14		±0.3	±0.4	±0.05	±10	±12	±4	$\pm 0.3 \times 10^{-2}$				
7008	S1234													
	inner	4.355797	3503.0	33.26	23.34	0.028	314	50613.62	1.397	5.73×10^{-3}			1.22	70
		±0.000007		±0.13	±0.19	±0.010	±18	±0.22	±0.012	$\pm 0.14 \times 10^{-3}$				
	outer	10360	1.1	33.26	3.4	0.65	148	44560	360		0.29	0.53	1.22	70
		±90		±0.13	±0.4	±0.04	±5	±140	±40		±0.05	±0.06		
					6.4				690		0.15		1.07	77
					±0.6				±50		±0.03			
10012	S796													
	inner	1910	2.5	33.88	1.28	0.45	208	55490	30	3.0×10^{-4}			0.33	28
		±31		±0.07	±0.20	±0.08	±13	±45	±5	$\pm 1.4 \times 10^{-4}$				
21005	S1278													
	inner	284.21	34.9	33.66	10.5	0.209	324	51979	40.0		0.150	0.92	1.10	32
		±0.08		±0.18	±0.3	±0.025	±7	±5	±1.0		±0.016	±0.05		
					11.4				43.6		0.138		2.29	32
					±0.6				±2.1		±0.010			

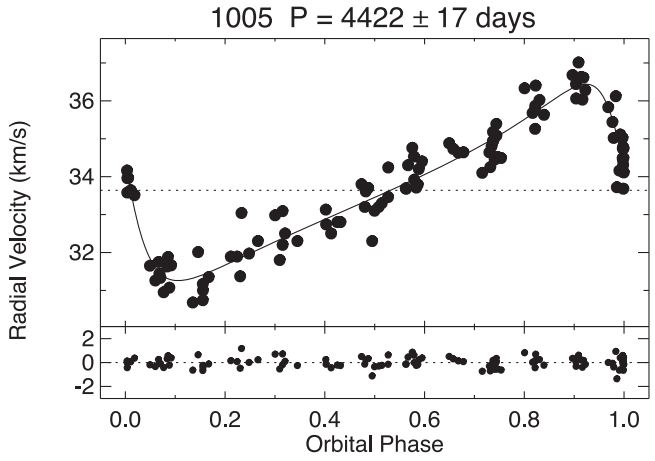

Figure 1. One example figure of 83 in total, showing a single-lined M67 member orbit plot of RV vs. phase. RV data points are shown with filled circles, and the orbital solution is plotted as a solid black line. The dotted line marks the γ velocity of the binary. Below each plot, the residuals ($O - C$) are given. Above each plot, we list the WOCS ID and orbital period.

(The complete figure set (83 images) is available.)

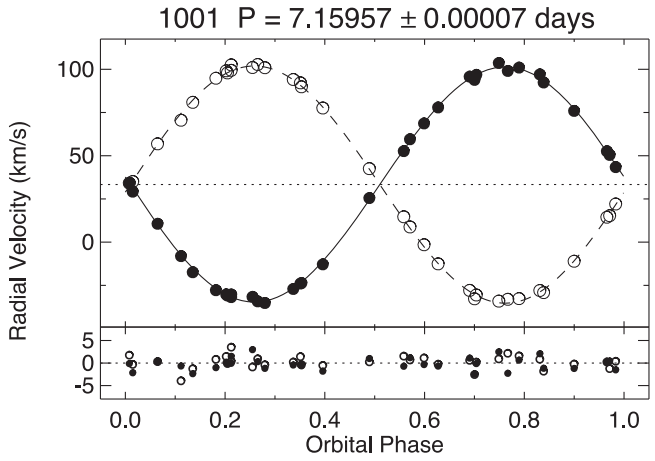

Figure 2. One example figure of 31 in total, showing a double-lined M67 member orbit plot. RV is plotted vs. phase, with primary RVs shown as filled circles and secondary RVs as open circles. The primary orbital solution is shown as a solid black line, the secondary solution as a dashed black line, and the dotted black line marks the γ velocity of the binary. Below each plot, the primary and secondary residuals ($O - C$) are given. Above each plot, we list the WOCS ID and orbital period.

(The complete figure set (31 images) is available.)

details and for the precisions of other data sources). Candidate orbit solutions not meeting these criteria have either small orbital amplitudes, insufficient phase coverage, or simply too few observations. Most of the solutions presented here are very clearly secure; but those with high eccentricities should be treated with caution if phase coverage at periastron is sparse.

3.1. Single-lined Binaries

Single-lined spectroscopic binaries (SB1s) are RV-variable stars with only one distinguishable peak in their cross-correlation functions. The orbital parameters for SB1s are presented in Table 2, and the corresponding plots of the orbital solutions are presented in Figure 1. For each SB1, in Table 2 we list its WOCS ID ("ID"), a cross-reference ID ("XID," see above), orbital period (P), number of orbital cycles covered in our data, center-of-mass RV of the binary (γ), RV semiamplitude of the orbital solution (K), eccentricity (e), longitude of periastron (ω), the Julian date of periastron (or maximum primary velocity, for circular orbits) nearest to the average date of observations (T_0), projected semimajor axis ($a \sin i$), mass function ($f(m)$), rms of the velocity residuals from the orbital solution (σ), and number of RV measurements (N).

3.2. Double-lined Binaries

Double-lined spectroscopic binaries (SB2s) are RV-variable stars with two distinguishable peaks in their cross-correlation functions. We extract primary and secondary RVs from SB2 spectra using the TwO-Dimensional CORrelation, TODCOR (Zucker & Mazeh 1994). We have two independent implementations, one a code by G.T. used for the CfA data, the other by A.G. used by the WOCS team. An advantage of TODCOR is that the templates for the primary and secondary stars can be optimized to match the observed spectra. The CfA code uses a library of synthetic templates (Goldberg et al. 2002; Latham et al. 2002). The WOCS code can also use a similar library of synthetic templates, but for this work, we choose to simply use the same high signal-to-noise ratio sky spectrum for the SB1 and SB2 (TODCOR) analyses of WIYN data. (The WOCS team has not found a significant improvement in the precision of RVs for these mostly solar-type and slowly rotating stars to justify using the more computationally intensive approach of the template grid for this project.) TODCOR simultaneously solves for the RVs of both the primary and secondary stars. This allows for precise measurement of RVs even in some cases where cross-correlation function peaks are highly blended. Our orbit-fitting procedure for SB2s involves first fitting an SB1 orbit to the primary RVs, then using the orbital parameters of that solution as initial guesses for an SB2 orbit fit (e.g., Goldberg et al. 2002; Geller et al. 2009). In Figure 2 we present orbital solutions for RV-member SB2s for which we were able to obtain reliable RV measurements of both the primary and secondary peaks. The parameters of these orbits are listed in Table 3 and follow the same format as Table 2, except that instead of the mass function $f(m)$, we provide the $m \sin^3 i$ values for both the primary and secondary, along with the mass ratio $q = m_2/m_1$.

Finding a reliable orbital solution for double-lined binaries is complicated by increased RV measurement errors due to blending and the lower signal-to-noise ratio of the secondary spectrum. For these reasons, SB2 σ values are typically somewhat higher than SB1s, particularly for the orbital parameters for the secondaries.

3.3. Triple Candidates

R10 found that about 10% of the targets in a volume-limited sample of 454 nearby solar-type stars are actually triple systems, composed of three stars in bound orbits. Indeed, triples are observed to be abundant within short-period binary samples (Tokovinin et al. 2006). We have identified six members of M67 that appear to be hierarchical triples. (The lower observed triple fraction in M67 as compared to that of the field may simply be due to our study only including RV triples; nonetheless, this would be an interesting topic for follow-up investigations.) For three of the M67 candidate triple systems we have solved for both the inner and the outer orbits,

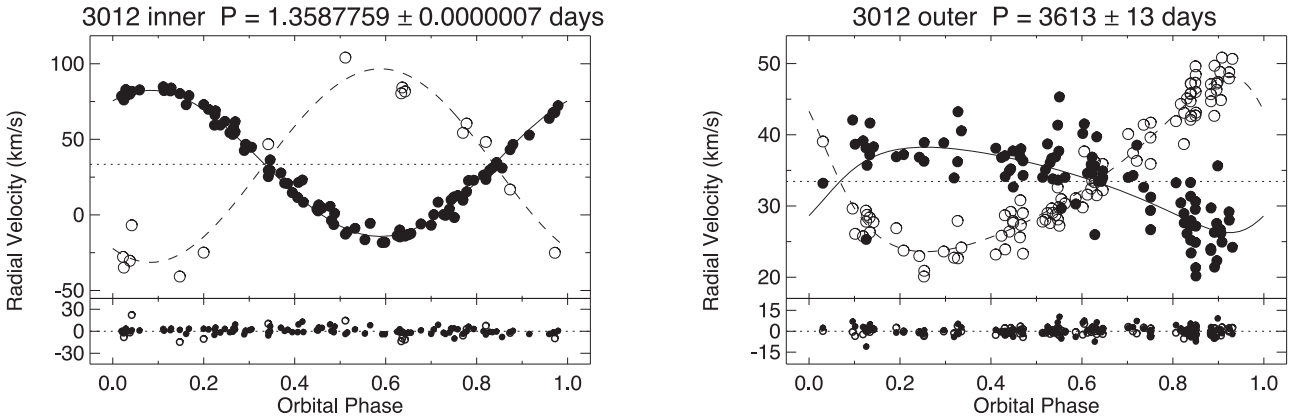

Figure 3. One example figure of six in total, showing an M67 triple member orbit. RV is plotted vs. phase, with primary RVs shown as filled circles and secondary RVs as open circles (where relevant). For two triples (WOCS 3012 and WOCS 7008), the outer orbits are fit using center-of-mass RVs of the inner binary and secondary RVs of the outer triple companion. These center-of-mass RVs are plotted with filled circles. The primary orbital solution is shown as a solid black line and the secondary solution as a dashed black line (where relevant). The dotted black line marks the γ velocity of the system. Below each plot, the primary and secondary residuals ($O - C$) are given. Above each plot, we show the WOCS ID, the component of the triple, and the orbital period.

(The complete figure set (6 images) is available.)

thus demonstrating that these system are bound. For the other three system we have solutions for the inner orbits, and evidence for an outer orbit with a period much longer than the span of our observations. The orbital parameters and plots for these triple systems are provided in Table 4 and Figure 3. They follow a similar format as for the SB1 and SB2 binaries. We also describe each triple in greater detail below.

WOCS 3012 (S1077)—This is a hierarchical triple-lined system with a simultaneous solution for the inner and outer orbits. There are 57 observations from the CfA DSs, 29 from WIYN/Hydra, and 16 from TRES. The primary is the brighter star in the inner binary, the secondary is the distant third star, and the tertiary is the faint companion in the inner binary. Velocities for all three stars were extracted from the TRES spectra using TRICOR (Zucker et al. 1995). There are hints of the tertiary in the WIYN/Hydra correlation plots, but no attempt was made to extract velocities beyond using TODCOR for the primary and secondary. Also for the DS observations, only primary and secondary velocities using TODCOR were extracted. We derived the orbital solutions of this system in two steps. Initially, we used the TODCOR velocities for the primary and secondary from all three sets of observations to solve for the inner and outer orbits simultaneously, using the code `dst` developed by G.T. This provided a good starting point for a TRICOR analysis of the TRES observations. We then combined all the velocities using a second code, `tst1` also developed by G.T., and including the TRES TRICOR velocities for the faint tertiary in order to derive a mass ratio for the inner binary.

WOCS 4008 (S2206)—This system has 91 observations with the CfA DSs, but no observations with WIYN/Hydra or TRES. The spectrum is clearly double-lined in a few of the DS observations, but most of the time, the primary and secondary peaks of the correlation function are blended. The best template for the primary is slightly evolved and cooler than a slightly hotter main-sequence template for the secondary. There is no evidence for variation in the velocity of the secondary, which is constant at 37.0 km s^{-1} with an rms of 1.6 km s^{-1} (see Figure 3). The RVs of the primary yield an orbital solution with a period of $P = 18.377$ days and semiamplitude of $K = 12.28 \pm 0.63$ km s^{-1}, implying a minimum mass for the companion of about 0.2 $M_{\odot}$. The scatter of the velocity residuals is large, about 4 km s^{-1}, but there is no obvious trend in them. The center-of-mass velocity for the primary is $\gamma = 31.3 \pm 0.4$ km s^{-1}, 2.3 km s^{-1} lower than the cluster mean RV of 33.64 km s^{-1} reported in Paper I. The secondary is 3.4 km s^{-1} higher. One possible explanation might be that the two stars are not a bound triple system, but rather that they are two low-probability cluster members that by chance lie on the same line of sight. A more appealing explanation might be that they are a bound triple with a very long period for the outer orbit. Assuming that the γ velocity of the triple system is the same as the cluster mean, the mass ratio would be about 1.5, consistent with an inner orbit composed of a slightly evolved star and late-M dwarf companion, and an outer orbit around a main-sequence star near the cluster turnoff. We also note that Mathieu et al. (1990) performed a careful photometry analysis of this system and determined a similar physical description.

WOCS 4030 (S1416)—This is a hierachical triple system with 21 observations from the CfA DSs. All of the spectra are single lined. These 21 RVs yield solutions for the inner and outer orbits when solved simultaneously. The secondary in the inner orbit and the distant third star in the outer orbit are both too faint to yield velocities. The code `sst` developed by G.T. was used to derive solutions for the inner and outer orbits.

WOCS 7008 (S1234)—This is a hierarchical triple system with a simultaneous solution for the inner and outer orbits. Its architecture is the same as WOCS 3012 (S1077), except that the primary is the distant third star in the outer orbit and the secondary is the brighter star in the inner orbit. The companion in the inner orbit is too faint to yield velocities, so only TODCOR was used to extract velocities. There are 51 observations from the CfA DSs, 8 from WIYN/Hydra, and 18 from TRES. Seven of the DS exposures were too weak to yield TODCOR velocities for the secondary. We note that Mathieu et al. (1990) also analyzed this system and presented a similar physical description.

WOCS 10012 (S796)—This single-lined system has 28 WIYN/Hydra RVs. The impression from a visual inspection of the velocity history is a periodic variation of several thousand days on top of a slow drift upwards. An orbit with a period of 1884 days fits the data reasonably well, with an orbital semiamplitude $K = 1.3$ km s^{-1} and velocity residuals of $\sigma = 0.6$ km s^{-1}. The

residuals show a slow drift of 2 km s^{-1} over a period of 4826 days, with no obvious curvature. This is a good candidate for a bound triple with a long-period inner binary and a distant third star in a much longer period outer orbit. In order to fit an orbit to the inner system, we fit the following linear equation to these data: $RV = 3.5027 \times 10^4\, JD - 19.4531$. We then subtract this linear fit from our observed RVs, and fit an orbital solution. In Figure 3 we show this orbital solution and also the observed RVs, the fitted trend line, and the RVs resulting from subtracting this trend from the observations. The resulting orbital parameters are provided in Table 4, and the observed RVs are provided in Table 1. Accounting for this slow drift in the residuals reduces the velocity residuals on the orbital solution to $\sigma = 0.33$ km s^{-1}.

WOCS 21005 (S1278)—This is a double-lined system with 12 recent TRES observations, 16 early CfA DS observations, and 5 WIYN/Hydra observations that sit in the gap between the CfA data sets. The orbital solution using all of the data (and included in Table 4 and Figure 3) has residuals of 1.1 and 2.2 km s^{-1} for the primary and secondary stars, respectively. Using only the CfA TODCOR velocities yields a similar orbit with velocity residuals of only 0.82 and 1.75 km s^{-1}. Inspection of the phased velocity plot for the orbital solution suggests that the WIYN/Hydra velocities are systematically shifted to higher values, and this is confirmed by plots of the residuals versus time, which show a shift on the order of 2 km s^{-1} (see Figure 3). This shift is much too large to be a systematic error in the WIYN/Hydra velocities, and a straightforward explanation is that we are seeing curvature in the velocities due to the pull of a distant third star in a bound outer orbit with a period several times longer than the time span of the observations.

3.4. Notes for Specific Binaries

WOCS 4021 (S815)—This SB1 binary is highly eccentric ($e = 0.83 \pm 0.07$). We do not have observations precisely at periastron; the uncertainties on the orbital semiamplitude derived from the orbit fit (and provided in Table 2) can likely be substantially reduced with future timely observations.

WOCS 10025 (S628)—This system is an SB2, where at least one star appears to be rotating rapdily. Determining which star is the primary and which is the secondary in each observation has proven to be challenging. Our best attempt (included in Table 1) results in primary RVs that span a range of ~30 km s^{-1}, and secondary RVs that span a range approaching 100 km s^{-1}. We have not been able to derive a reliable orbit solution.

WOCS 13004 (S1011)—This SB1 binary appears to have an orbital period of ~14,620 days, and it is included in Table 2 and Figure 1. However, we caution the reader that we have only covered 80% of the orbital phase, and so the orbital elements may be uncertain and subject to change once observations covering the full orbit are obtained and included in the fit.

Photometric variables and X-ray sources—In Table 5 we provide a list of the known photometric variables and X-ray sources for which we have RV orbital solutions. The column labeled "ID" provides the WOCS ID, and the column "XID" provides a cross-match ID (in the same format as Table 1, and here mostly from Sanders 1977). Within the "Notes" columns, X-ray sources identified by Belloni et al. (1998) with ROSAT are labeled "X," followed by the source number given in their paper. Likewise, X-ray sources identified by VandenBerg & Stetson (2004) with Chandra are labeled "CX", followed by the source number given in their paper. We draw our sample of photometric variables from a number of references, provided in Paper I, and label them "PV," or "PV?" if the authors identify the photometric variability as uncertain. We also provide the GCVS names for photometric variables where available (e.g., HT Cnc, EV Cnc, etc.).

Table 5
Photometric Variables and X-Ray Sources with RV Orbital Solutions

ID	XID	Notes
1001	S1024	SB2, PV, CX111
1015	S1237	SB1, X52, CX47, YG
2002	S1040	SB1, PV, X10, CX6, YG
2003	S1045	SB2, PV, X41, CX88
2008	S1072	SB1, X37, CX24, YG
2016	M6176	SB1, PV?
3004	S1264	SB1, PV?
3012	S1077	SB2, triple, PV, HT Cnc, X7, CX10
4001	S1029	SB1, PV
4003	S1036	SB1, RR, PV, W UMa, EV Cnc, X45, CX19
4007	S986	SB1, PV, HV Cnc, CX157
4016	S1224	SB2, PV?
5037	S1508	SB1, PV
6005	S999	SB2, PV, HW Cnc, X13, CX9
6008	S1242	SB1, PV, X50, CX49
6010	S1272	SB2, CX155
6016	S760	SB1, X49
7002	S1019	SB2, PV, X11, CX5
7008	S1234	SB2, triple, X53, CX36
7022	S745	SB1, PV
9011	S773	SB1, CX72
11022	S1109	SB1, PV
12004	S1009	SB1, CX78
13008	S1063	SB1, PV, HU Cnc, X8, CX1, SSG
14007	S1070	SB2, PV, HX Cnc, X38, CX48
15028	S1113	SB2, PV, X26, SSG
17004	S1050	SB1, CX104
21006	S996	SB2, CX81
24021	S819	SB2, PV, HR Cnc, CX58

Candidate binaries without orbital solutions—Table 6 contains velocity variables that we identified as binaries (having $e/i \geqslant 3$), but for which we do not yet have orbital solutions. (The e/i value measures the spread in RVs relative to the expected precision of the RVs; see Paper I and Geller et al. 2008 for more details.) In this table, we include the WOCS ID (column "ID"), a cross-match ID ("XID"), the "class" (see Paper I), the e/i value, and the time span of our observations (ΔJD, in days) as a possible lower limit to the true orbital period. (Where necessary, all values have been updated from Paper I to include the current set of observations in Table 1.) The RV memberships for all of these binaries are somewhat uncertain because we do not yet know the center-of-mass RV for each system. However, all of these are PM members.

Candidate low-amplitude and/or long-period binaries—Table 7 and Figure 4 contain stars that do not pass our criteria for RV variability of having $e/i \geqslant 3$, but show an obvious trend of RV versus time when visually inspected. The columns in the table are the same as in Table 6, but we exclude the "class" column (because all are classified as "single members," SM). For statistical purposes, we include these stars as RV nonvariables (i.e., "singles") in our binary frequency analysis in Section 5, as they should be accounted for in our incompleteness correction. Additional precise RV

Table 6
Candidate Binaries without Orbital Solutions

ID	XID	Class[a]	e/i	ΔJD
4017	S1463	BU	3.33	17242.8
5032	S1406	BLM	4.15	5177.4
6025	S1431	BLM	10.78	5178.4
8004	S2219	BLM	4.65	11756.0
9029	S1604	BLM	4.62	5179.1
10018	S1462	BLM	4.22	5178.4
10024	S1432	BU	12.30	5179.2
10025[b]	S628	BU	14.42	5468.3
11043	S1579	BLM	14.74	2274.8
12032	S1405	BLM	7.37	4845.1
13013	S1251	BLM	4.87	11350.3
14012	S965	BLM	8.21	11020.1
14025	S1112	BLM	31.97	4822.0
16024	Y589	BLM	3.29	4819.8
16029	S636	BLM	5.07	4336.1
16036	S1179	BLM	5.75	5030.2
19020	S800	BU	3.87	11334.4
19032	M6452	BLM	8.58	1896.1
20059	S243	BU	25.97	2281.7
21036	S637	BU	19.46	2273.7
21037	F4146	BLM	3.94	1536.8
21044	F2832	BLM	26.30	1896.1
23015	M5821	BLM	62.98	1892.1
23026	M6441	BLM	74.87	1898.1
24007	S1286	BLM	6.03	11350.3
24012	S797	BU	21.54	5135.2
25008	S1042	BU	12.78	5135.2
25013	S764	BU	6.63	5179.1
25039	S1709	BLM	41.52	5179.1
27011	M5380	BLM	7.96	5179.1
28008	F3467	BLM	6.89	5178.1
28028	M5285	BU	26.92	2153.1
28059	S250	BLM	5.00	4827.8
34046	F5460	BLM	15.64	1538.8

Notes.
[a] Specifically, the classification "BLM" is for "binary likely members"; these binaries have both RV and PM membership probabilities $\geqslant$50% (see also Paper I for how we incorporate the multiple PM surveys; here we have also accounted for Gaia PMs). The classification "BU" is for "binary with unknown membership"; these binaries are PM members, but the RV membership calculated from the mean value of the current RVs is <50%. We include BU binaries in our member sample because M67 has excellent PM information. These binaries are included in our binary frequency analysis and are accounted for by our incompleteness analysis in the orbital parameter distributions below.
[b] WOCS 10025 has a double-lined spectrum; we show the e/i value and class derived from the primary velocities.

observations will be important to derive orbital solutions for these binaries.

4. Completeness in Binary Detection and Orbital Elements

In Section 2 we discussed our sample selection, and further details are available in Paper I along with information on the completeness of our survey. In short, we have derived RV membership probabilities and characterized the RV variability of ∼91% of our complete stellar sample (down to $V = 16.5$) and >99.5% of the stars in our sample with $V < 15.5$. We find a total of 604 cluster members, 169 of which show significant RV variability ($e/i > 3$). However, our RV survey is likely not sensitive to all binaries in the cluster.

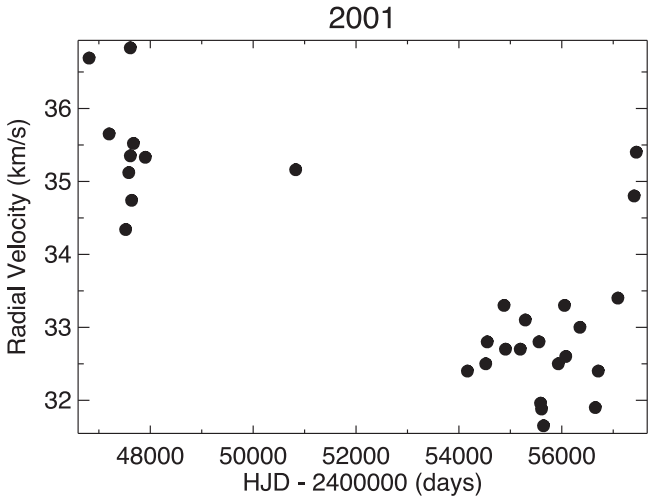

Figure 4. One example figure, out of 22 in total, showing a candidate M67 binary that visibly shows a low-amplitude trend in RV vs. time, but is not identified as a binary in our statistical analysis (see Table 7). We show the observed RV vs. time as filled black circles and provide the WOCS ID above. (The complete figure set (22 images) is available.)

Table 7
Candidate Low-amplitude Binaries

ID	XID	e/i	ΔJD
2001	S1027	1.34	10639.0
2004	S1016	1.27	13424.3
3107	S80	1.39	12785.1
4015	S1456	0.81	11663.1
5004	S2212	1.88	16870.9
5020	S1458	1.77	8704.2
5025	S827	1.50	10252.3
5026	S1337	1.20	10158.2
5051	S368	0.39	11667.2
5058	S341	0.90	9105.1
5066	S671	0.69	10602.0
6011	S775	1.14	14730.9
6023	S618	1.13	10189.1
7005	S1274	0.81	11791.9
7014	S1092	2.31	8761.1
8005	M5951	1.40	10610.9
10005	S2208	1.24	12064.9
10026	S1470	2.54	1747.3
13012	S1218	1.81	10546.0
15009	S991	1.60	11293.1
15010	S1252	0.88	10229.1
27035	F4898	2.18	1393.2

For example, the maximum baseline of RV observations for a given star in our survey is $\sim 10^4$ days. Binaries in the galactic field have periods extending well beyond this time span (R10). In a star cluster, dynamical encounters will break up binaries at periods beyond the "hard-soft boundary" (Heggie 1975). Using the virial theorem and assuming the velocity dispersion is isotropic with a one-dimensional velocity dispersion for solar-type main-sequence stars in M67 of $0.59^{+0.07}_{-0.06}$ km s^{-1} (Paper I), we estimate that the orbital period at the hard-soft boundary in M67 for solar-mass stars is approximately 10^6 days. Therefore all of the binaries in our sample are hard. Furthermore, there are assuredly binaries in M67 that we have not detected because they have long periods, high eccentricities, and/or low mass

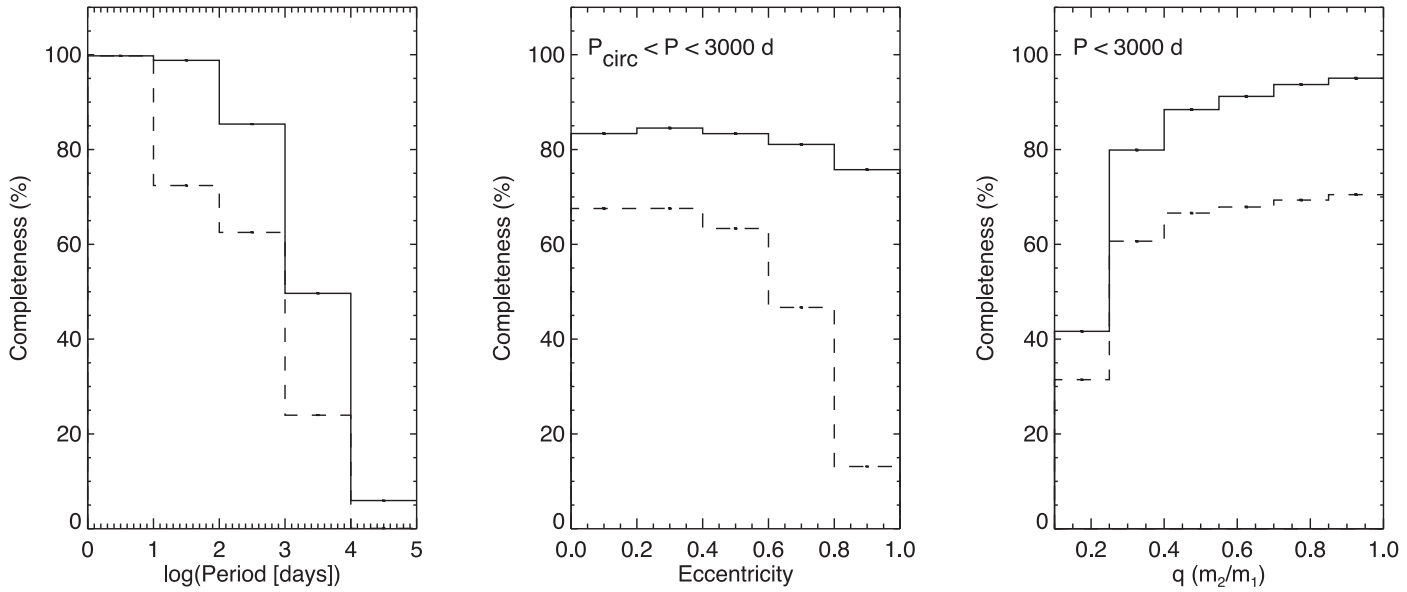

Figure 5. Completeness in binary detection (solid lines) and binary orbits (dashed lines) as a function of period (left), eccentricity (middle), and mass-ratio (right).

ratios that are beyond the detection limits of our observational survey.

To estimate the completeness of our survey, we follow a similar method as in GM12 and updated in Paper I. Briefly, we run a Monte Carlo analysis to generate a population of synthetic binary stars that follow the M67 binary primary-mass distribution (as estimated relative to a 4 Gyr isochrone) and the orbital-parameter and mass-ratio distributions of the solar-type galactic field binaries from R10. We produce synthetic RVs for these binaries on the true observing dates of our M67 survey, using realistic RV uncertainties for observations from each telescope (see Paper I). We then analyze these RVs in the same manner as our real observations.

A synthetic binary is considered detected if the e/i value is $\geqslant 3$, as we also defined for our observationally detected binaries in Paper I. Using this method, we conclude that within our magnitude and spatial limits we have detected 74% of the binaries out to a period of 10^4 days in M67. For orbital periods beyond 10^4 days, our detection completeness drops precipitously (Figure 5).

To estimate our completeness in binary orbital solutions, we use the same software as we used in this paper to derive the orbital solutions from our true observations, but here with RVs from our synthetic binaries. As in GM12, we consider an orbital solution acceptable in these simulations if it has RVs covering at least one period, errors on P, e, and the orbital semiamplitude K smaller than 30% of the derived values, an rms residual velocity lower than 1 km s^{-1}, and a range in RVs covering at least 75% of the orbital amplitude (mainly applicable for highly eccentric binaries).

The results of this completeness analysis are shown in Figure 5. Given the similar survey duration and methods as in GM12 for NGC 188, our completeness curves look very similar to Figure 1 in GM12. We estimate that for orbital periods of < 3000 days, we have derived orbital solutions for $\gtrsim$50% of our sample. Beyond 3000 days, our completeness quickly drops to zero (reaching nearly 0% at $> 10^4$ days). For much of the binary orbital parameter analysis presented below, we therefore limit our investigation to binaries with periods < 3000 days.

5. The Main-sequence Hard-binary Frequency

We define a main-sequence sample as those stars with $V < 15.5$, $(B-V) > 0.5$ and $V > 8.4 \times (B-V) + 7.25$ (using the photometry in Paper I, which is mostly drawn from Montgomery et al. 1993). The faint limit of $V < 15.5$ is set by our observational completeness (see Paper I). The blue limit excludes potential blue stragglers that have not already been identified in Paper I. The last condition was determined by eye to include the main-sequence locus up through the turnoff. (For reference, see the color–magnitude diagram in Figure 8 of Paper I.) Following a similar method to GM12, we also exclude the few binaries from this frequency analysis that after correcting for secondary light, would have primaries with $V \geqslant 15.5$.

Of the 400 main-sequence stars in our sample of M67, we identify 101 binaries. When corrected for incompleteness out to an orbital period limit of 10^4 days, this results in a main-sequence hard-binary frequency of $34\% \pm 3\%$.

For comparison, when we limit the NGC 188 sample to the same (physical) radial extent as our M67 sample, we find a solar-type main-sequence binary fraction of $32\% \pm 4\%$ out to orbital periods of 10^4 days, nearly identical to that of M67.

In Figure 6 we divide the main-sequence sample in bins of radius to compare the incompleteness-corrected binary frequency in the core to that in the halo. In each bin, we run our Monte Carlo completeness analysis as described above, and find a similar detection completeness of $\sim$74% (out to orbital periods of 10^4 days) in each bin. Inside about 0.4 core radii, the binary frequency reaches $70\% \pm 17\%$. Outside of 0.4 core radii, the binary frequency is nearly constant at about 30% to 40% to the limit of our survey.

The binaries in M67 are known to be centrally concentrated (Mathieu & Latham 1986, Paper I). Indeed, a rise in binary frequency toward the cluster center is expected as a well-known effect of mass segregation. Mass segregation in M67 has also been noted previously (e.g., Sarajedini et al. 1999, without distinction to binaries), and is also seen in other clusters (e.g., Mathieu 1985; Milone et al. 2012, GM12), and in

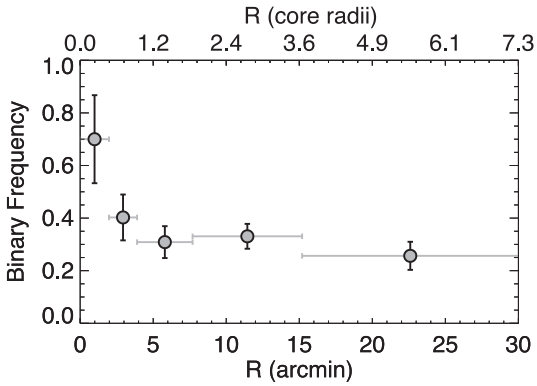

Figure 6. Binary frequency as a function of radius from the cluster center. We take equal bins in the log over our survey extent; horizontal bars extend to the respective bin edges. The points are corrected for observational incompleteness out to periods of 10^4 days; vertical bars show the uncertainties on our binary frequency measurements. We provide distances in arcmin and also converted into core radii using a core radius of $4\farcm12$ (Davenport & Sandquist 2010), which at a distance of 850 pc is equivalent to 1.02 pc.

N-body simulations of old open clusters (e.g., Hurley et al. 2005; Geller et al. 2013).

6. Binary Orbital Parameter and Mass Distributions

In the following subsections, we analyze the distributions of binary orbital parameters and secondary masses for the main-sequence binaries in our sample in M67. We exclude triples here, as their orbital elements (particularly for the inner binaries) may have been modified through internal dynamics during the cluster lifetime. We use our completeness analysis and also compare with theoretical and observed distributions, where appropriate. In particular, we compare with the main-sequence binaries in the old open cluster NGC 188, which also has a very thorough (and similar) analysis of the hard-binary population (GM12). We present the figures here with a statistical analysis, and save most of the discussion for Section 7.

6.1. Periods and Eccentricities

In the top panels of Figures 7 and 8 we show the distributions of orbital periods and eccentricities, respectively, for the M67 main-sequence binaries in our sample. The observations are shown in gray, with the incompleteness correction applied to the histogram (top panel) shown in solid lines with error bars.

Beginning with the period distribution (Figure 7), with the dashed lines we compare with a log-normal fit to the period distribution of the solar-type binaries in the galactic field from R10; specifically, this log-normal distribution has a mean value of $\log_{10}(P\,[\mathrm{days}]) = 5.03$ and $\sigma_{\log_{10}(P)} = 2.28$. In the top panel, we show this distribution in comparison to our incompleteness-corrected observations. In the bottom panel, we apply our observational incompleteness to the R10 log-normal distribution in order to compare directly with our observations.

A one-sample Kolmogorov–Smirnov (K-S) test comparing the M67 observations with this field log-normal distribution (with our incompleteness applied) returns a marginal distinction with a *p*-value of 5.0×10^{-3}, or 2.81σ. It appears that the M67 binaries may be marginally depleted at the longer periods as compared to the field; we return to this in Section 7. With the dotted line, we compare with a period distribution that is uniform in the log, as is often used in theoretical models (including the M67 *N*-body model of Hurley et al. 2005). A one-sample K-S test comparing the observations with the incompleteness-applied log-uniform period distribution returns a *p*-value of 7.6×10^{-5}, distinct at 3.96σ.

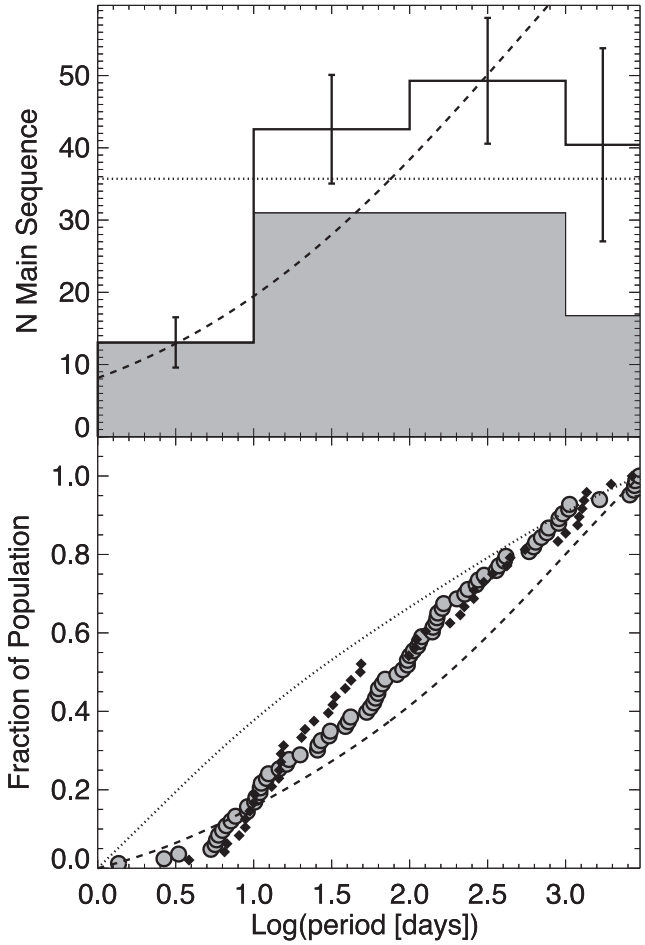

Figure 7. Period distribution for M67 main-sequence binaries in both histogram (top) and cumulative distribution (bottom) form. In gray we show the observed binaries in M67. In the top panel, we apply our incompleteness correction in the solid-lined histogram. In both panels, we plot (for reference) the log-normal period distribution from the solar-type binaries in the field (R10) as the dashed line, and also a log-uniform distribution that is commonly used in theoretical models as the dotted line. In the top panel, these lines are normalized such that the integral below the curves produces the incompleteness-corrected number of M67 binaries in this sample. In the bottom panel we apply our observational incompleteness to these curves in order to compare directly to our measurements. Also in the bottom panel, we show the cumulative period distribution from the old open cluster NGC 188 as black squares (GM12).

In the bottom panel of Figure 7 we also compare with the observed binaries in NGC 188 from GM12. The NGC 188 survey has very similar completeness as our M67 survey, and therefore we do not apply any correction to the NGC 188 data. A two-sample K-S test comparing the NGC 188 and M67 observations returns no significant distinction (with a *p*-value of 0.60).

Turning to orbital eccentricity, we plot in Figure 8 the eccentricity distribution for the subset of M67 (and NGC 188) binaries with periods between the circularization period and 3000 days. In this figure, we compare with both a uniform distribution (dashed line, as suggested for the galactic field solar-type binaries with periods beyond the circularization

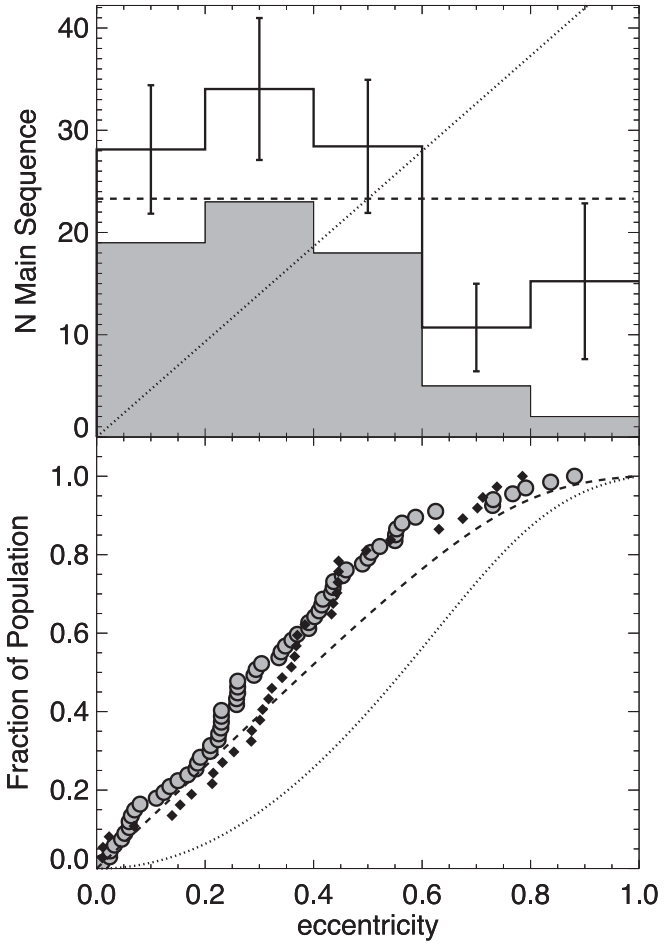

Figure 8. Eccentricity distribution for the M67 main-sequence binaries in the same format as in Figure 7. Here we only show binaries with periods between the tidal circularization period (see Section 6.2) and 3000 days. We compare with a uniform distribution (dashed line), consistent with solar-type binaries in the field (R10), and a thermal distribution (dotted line), as is often used in theoretical models. In the bottom panel, both of these lines have our observational incompleteness applied so that they can be compared directly with our observations. As in Figure 7, we show the cumulative eccentricity distribution from the old open cluster NGC 188 in the bottom panel as black squares (GM12).

limit; R10), and a thermal distribution (dotted line; Jeans 1919; Ambartsumian 1937; Heggie 1975). The thermal distribution is often used in theoretical models because it is elegant and simple, but there is little support for this distribution from observations (GM12, Duchêne & Kraus 2013; Moe & Di Stefano 2017; Geller et al. 2019). A one-sample K-S test comparing the M67 observations to the incompleteness-applied thermal distribution returns a p-value of 2.9×10^{-11}, distinct at 6.65σ. On the other hand, a one-sample K-S test comparing the M67 observations to the incompleteness-applied uniform distribution returns no significant distinction (with a p-value of 0.046).

We also compare the M67 eccentricity distribution to that of NGC 188 in the bottom panel of Figure 8. A two-sample K-S test comparing these two observed samples returns no significant distinction (with a p-value of 0.38). In summary, the M67 main-sequence binary eccentricity distribution is consistent with that of similar binaries in NGC 188 and the field, and can be described by a uniform distribution.

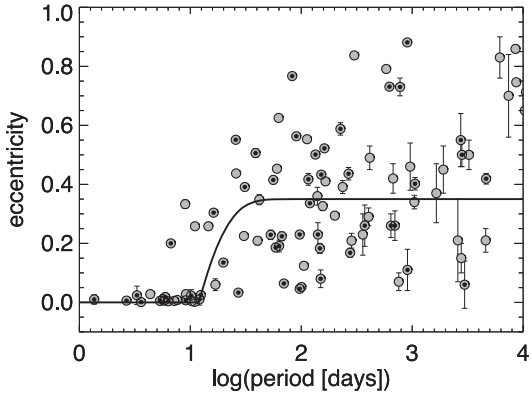

Figure 9. The period-eccentricity ($e - \log P$) distribution of M67 main-sequence binaries. Error bars are drawn for all orbits, although in many cases these are smaller than the points themselves. The points with filled black circles in the interior mark the unevolved main-sequence binaries used in fitting for the circularization period ($P_{\rm circ}$). The black line shows our fit of the circularization function from MM05, resulting in $P_{\rm circ} = 11.0^{+1.1}_{-1.0}$ days.

6.2. Tidal Circularization

The rate of tidal circularization depends on the strength of the tidal force, which scales as the inverse cube of distance. Consequently, within coeval populations such as open clusters, nearly all main-sequence binaries of similar primary mass below a characteristic orbital period are found to be circular. As the population ages and wider binaries finish circularizing, this circularization period ($P_{\rm circ}$) increases to longer orbital periods (Mayor & Mermilliod 1984; Meibom & Mathieu 2005, hereafter MM05).

Mathieu & Mazeh (1988), Latham et al. (1992), and MM05 studied the circularization period in M67 using a subset of the binaries included in our study. We revisit the circularization period here using our larger binary sample. Notably, our study extends further down the main sequence, allowing us to select a sample of stellar binaries that is less affected by the rapidly increasing radius near the cluster turnoff. Specifically, we use the subset of M67 main-sequence binaries with $V > 13.5$. This bright magnitude limit is approximately where the main sequence detaches from the zero-age main sequence (ZAMS; see Figure 8 in Paper I). We also exclude the candidate triples discussed Section 3.3 and the blue lurkers introduced by Leiner et al. (2019). Our aim is to include only unevolved main-sequence binaries that have not undergone internal eccentricity evolution due to triple dynamics or mass-transfer processes. This sample includes 52 binaries, which are identified in the $e - \log P$ diagram of Figure 9.

We fit these data with the circularization function from MM05 (Equation (1) therein) in order to derive the circularization period. Our method differs slightly from that of MM05 as follows. We use an orthogonal distance regression method to fit the circularization function, which accounts for the uncertainties on both the period and eccentricity. We also employ a bootstrapping technique to derive a distribution of measured circularization periods. Specifically, in each of 10^5 iterations, we randomly select 52 binaries from this M67 binary sample with replacement, and derive the circularization period from this random sample. The resulting distribution of circularization periods is shown in the black-lined histogram in Figure 10.

The distribution shows two peaks, one at approximately 11 days and another at approximately 16 days. We choose to fit

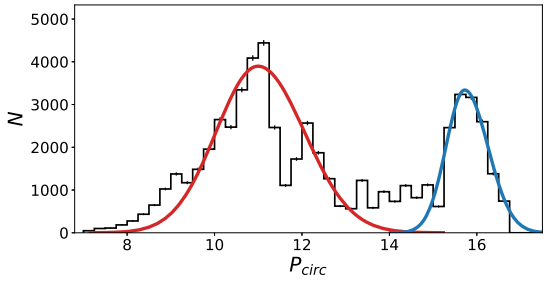

Figure 10. Distribution of circularization periods ($P_{\rm circ}$) resulting from our bootstrap analysis (black histogram), fit with two asymmetric Gaussian functions. The red curve shows the asymmetric Gaussian fit to the bulk of the distribution and results in $P_{\rm circ} = 11.0^{+1.1}_{-1.0}$ days. (The fit represented by the blue curve results in a value of $15.7^{+0.5}_{-0.4}$ days.)

an asymmetric Gaussian function to each of these peaks in the distribution (separately). Each asymmetric Gaussian is defined by a single mean and a single amplitude, but with two σ values, one on either side of the mean. We show the Gaussian fits to these two peaks in the red and blue curves (respectively). The portion of the distribution fit by the red curve has a far larger integrated area, and we therefore consider this the cluster circularization period, with a value of $P_{\rm circ} = 11.0^{+1.1}_{-1.0}$ days. (The uncertainties show the high and low 1σ values derived directly from the fitting function.) This circularization period is in agreement (to within the uncertainties) with that found by MM05 for M67 of $12.1^{+1.0}_{-1.5}$ days, who had a smaller sample and also included brighter binaries closer to the turnoff.

Statistically, the secondary peak at ~16 days arises from the few nearly circular binaries with somewhat longer periods in the sample, in iterations of the bootstrap technique that by chance also exclude some shorter-period binaries. Physically, it is not immediately clear what meaning should be given to this peak, although we note that a similar double-peaked distribution was recently seen (using a similar technique) in the spectroscopic binaries in NGC 7789 (Nine et al. 2020).

6.3. Secondary-mass and Mass-ratio Distributions

For all binary orbits, we can derive the mass function,

$$f(m) = \frac{m_2^3 \sin^3 i}{(m_1 + m_2)^2} = \frac{PK^3}{2\pi G}, \quad (1)$$

where m_1 and m_2 are the primary and secondary masses, respectively, i is the orbital inclination to our line of sight, P is the orbital period, and K is the RV semiamplitude of the orbit. P and K are known from our orbital solutions.

In Figure 11 we show the cumulative distribution of mass functions for the main-sequence binaries in our M67 sample (gray points). For comparison, we also show mass functions corresponding to binaries with secondaries drawn from a uniform mass-ratio distribution (dashed line) and from a Kroupa (2001) IMF (dotted line).

To generate these theoretical curves, we follow a similar procedure as in GM12, which requires an estimate of the distribution of primary masses in our binary sample. We estimate primary masses for the binaries using the BV photometry and a 4 Gyr Padova isochrone.

A one-sample K-S test comparing the observations with the uniform mass-ratio curve shows no significant distinction (with a p-value of 0.46). On the other hand, a similar K-S test

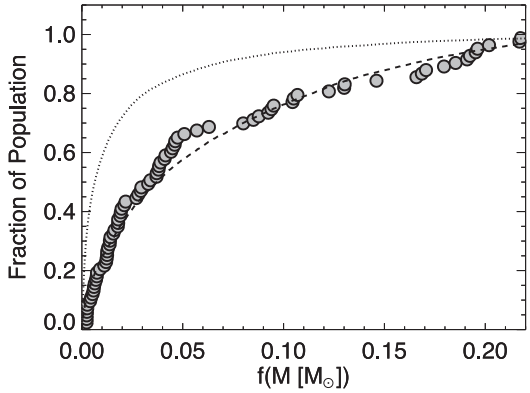

Figure 11. Distribution of mass functions for the M67 main-sequence binaries (gray dots). For comparison, we also show the mass-function distributions resulting from drawing primary masses from our observed distribution and mass ratios from a uniform distribution (dashed line) as well as secondary masses drawn from a Kroupa (2001) IMF (dotted line). Our incompleteness corrections have been applied to both model distributions.

comparing the observations with the IMF results in a p-value of 1.3×10^{-12}, a 7.10σ distinction.

In order to derive the distribution of secondary masses, we use the statistical algorithm of Mazeh & Goldberg (1992) to convert our distributions of mass functions and primary masses into the distributions of secondary masses and mass ratios for the M67 main-sequence binaries. (See GM12 for further details.) The results of this analysis are shown in Figure 12.

In Figure 12 the observations are shown in gray (with SB1s in vertically hatched regions and SB2s in horizontally hatched regions), and the incompleteness-corrected distributions are shown as solid lines with error bars. For comparison, we also plot curves showing a uniform mass-ratio distribution (dashed lines) and the Kroupa (2001) IMF (dotted lines), normalized to our observed M67 sample size. To construct the dashed line in the top panel, we draw primaries from our observed primary-mass distribution and mass ratios from a uniform distribution to obtain a distribution of secondary masses defined by a uniform mass-ratio distribution. The downturn in this distribution toward higher secondary masses is due to a similar downturn in the primary-mass distribution. In the bottom panel, to derive the dotted line, we first draw primary masses from our observed primary-mass distribution, then secondary masses from the IMF up to the mass of the respective primary mass (thereby forcing the mass ratio to be lower than unity), and we then plot the resulting mass-ratio distribution.

Although we do not use these plots for a quantitative comparison (as we prefer a comparison to the observed mass functions instead), we can see a similar result by eye, as is shown in Figure 11. Qualitatively, (dashed) lines resulting from the uniform mass-ratio distribution follow the observed distributions more closely than those resulting from the IMF.

We do not observe a strong peak at mass ratios of unity in M67 (or NGC 188, see Figure 13). Interestingly, such "twin" binaries are abundant in solar-type stars in the field. For example, the field binary mass-ratio distribution in R10 (their Figure 16) shows a peak at $q \sim 1$ that is approximately twice as high as the bins at lower mass ratio (although we note that their bin sizes are much smaller than those we use here in Figure 12).

Finally, in Figure 13 we compare the M67 incompleteness-corrected secondary-mass and mass-ratio distributions (in black) directly to those of NGC 188 (in gray, from GM12).

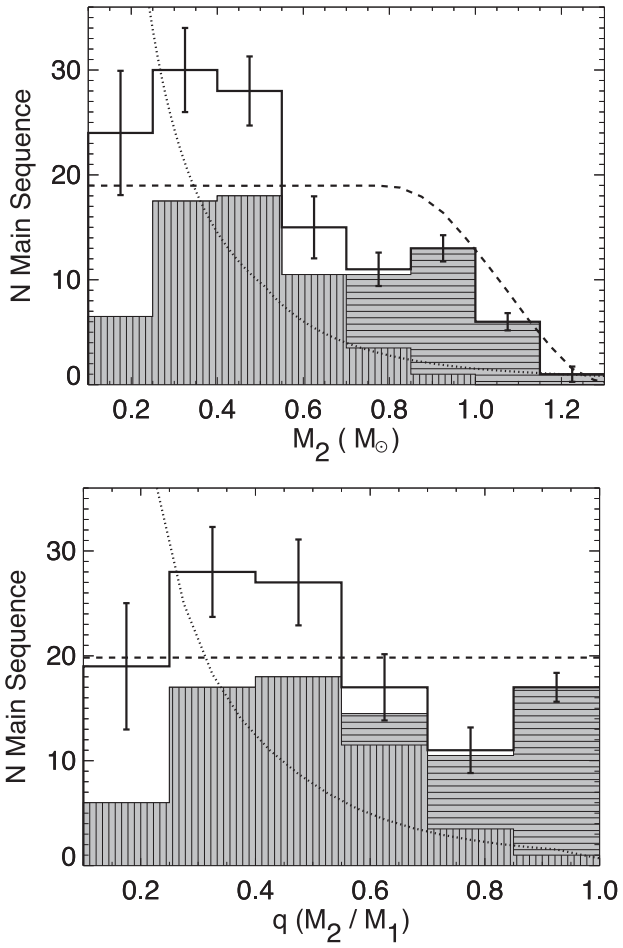

Figure 12. Distributions of secondary masses (top) and mass ratio (bottom) of M67 main-sequence binaries, estimated with the statistical algorithm of Mazeh & Goldberg (1992). The observations are shown in gray, with SB1s in vertically hatched regions and SB2s in horizontally hatched regions. The incompleteness-corrected distributions are shown as solid lines. For comparison, in the top panel we also plot a Kroupa (2001) IMF (dotted line) and the secondary-mass distribution that results from a uniform mass-ratio distribution (dashed line, see main text for details). With the dotted line in the bottom panel, we show the mass-ratio distribution resulting from choosing secondaries from the IMF and primaries from our observed M67 primary-mass distribution. Finally with the dashed line in the bottom panel, we show the uniform mass-ratio distribution.

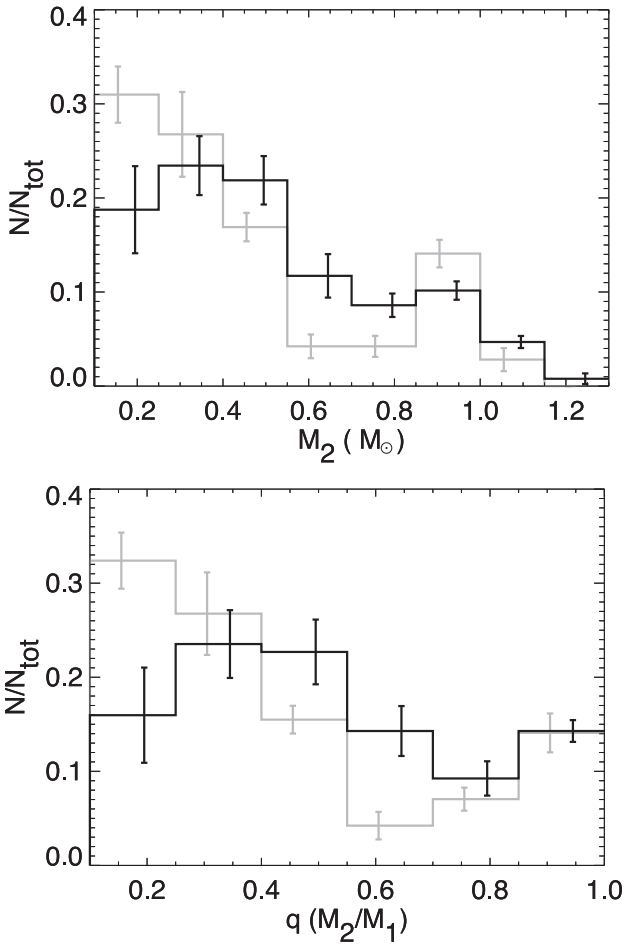

Figure 13. Distribution of secondary masses (top) and mass ratios (bottom) of the main-sequence binaries in M67 (black) in comparison to the main-sequence binaries in the open cluster NGC 188 (gray). We show only the incompleteness-corrected distributions here. Error bars are shifted slightly off-center from each bin for clarity.

Here we do not compare using the mass functions because our observations in each cluster sample a slightly different primary-mass regime. The shapes of the NGC 188 and M67 secondary-mass distributions are qualitatively similar (both rising toward lower masses), as is also true for the mass-ratio distributions (both showing some evidence of a rise toward lower mass ratios). However, formally, a χ^2 test comparing the M67 and NGC 188 secondary-mass distributions or mass-ratio distributions results in $>3\sigma$ distinctions, respectively. We return to this in the following section.

7. Discussion

In the previous sections we compared the properties of solar-type main-sequence binaries in M67 to similar binaries in the older (7 Gyr) open cluster NGC 188 and the field. In this section we synthesize these results in the context of star-cluster dynamical evolution.

When we investigate the binary fraction of the solar-type main-sequence binaries in the field (R10) out to the same limiting orbital period as for M67 (10^4 days), we find a binary fraction of $19\% \pm 2\%$. The M67 solar-type main-sequence binary fraction out to the same period cutoff is significantly (4.27σ) higher than this at $34\% \pm 3\%$. The NGC 188 solar-type main-sequence binary fraction within the same period and physical radius of 7 core radii is nearly identical to that of M67 at $32\% \pm 4\%$.

Solar-type binaries in two additional WOCS clusters, M35 (NGC 2168; 150 Myr) and NGC 6819 (2.5 Gyr), have also been surveyed at a similar level of completeness as M67 and NGC 188. Leiner et al. (2015) find M35 to have a main-sequence binary fraction out to the same period limit and within $\sim$4 core radii of $24\% \pm 3\%$. Milliman et al. (2014) find NGC 6819 to have a main-sequence binary fraction out to the same period cutoff and within $\sim$12 core radii of $22\% \pm 3\%$. These open cluster binary fractions are all statistically consistent. A more careful comparison that accounts for the different spatial extents of each survey is of interest, in particular to investigate for any trends in binary fraction with cluster age or other parameters; however, that level of analysis is beyond the scope of this paper.

Turning to the period distribution, M67 shows a marginal (2.81σ) distinction from that of the field, driven primarily by

the lack of long-period binaries in our sample. On the other hand, the distributions of orbital periods in M67 are consistent with those in NGC 188.

The eccentricity distributions for main-sequence binaries with periods between the circularization period and 3000 days in M67, NGC 188, and the field are all consistent with a uniform distribution (and inconsistent with a thermal distribution).

Turning to the observed distribution of mass functions, our M67 sample is consistent with mass ratios drawn from a uniform distribution, as is also observed for solar-type main-sequence binaries in NGC 188 and the field. We do not observe an abundance of twin ($q = 1$) binaries in M67 or NGC 188, in contrast to the results of R10 for the field. However, comparing the incompleteness-corrected mass-ratio and secondary-mass distributions of NGC 188 and M67 suggests that M67 lacks binaries with low-mass companions compared to NGC 188.

One explanation for these subtle differences between the M67 binaries and these two comparison samples could simply be differences in the progenitor binary populations, perhaps due to formation processes. Another explanation could be that they were born with similar binary properties and that dynamics subsequently modified them.

Indeed, the results of these comparisons are consistent with expectations of cluster dynamics. The larger binary fraction in our M67 (and NGC 188) sample compared to the field may be due to single stars, which have lower masses on average than the binaries, being preferentially lost from the cluster, or preferentially located at larger radial extent, due to two-body relaxation and mass-segregation processes (as was also discussed in GM12 for NGC 188). The lack of long-period binaries compared to the field may be due to the long-period binaries being "hardened" toward shorter periods. The lack of low-mass companions among the M67 binaries compared to NGC 188 may be tied to the difference in radial extent of our samples and to the processes of mass segregation and dynamical encounters. The NGC 188 sample extends to ∼13 core radii, while the M67 sample is limited to ∼7 core radii. Mass segregation leads to binaries with lower mass companions likely having larger radial distributions. Moreover, cluster cores are generally the densest regions of the cluster, where encounters are most frequent; exchange encounters tend to drive binaries closer to mass ratios of unity.

8. Summary

In this paper we expand upon the M67 RV study of Paper I by presenting orbital solutions for 120 solar-type binary- and triple-star cluster members in M67 (4 Gyr). Our full stellar sample spans a primary-mass range of ∼ 0.7–1.3 $M_{\odot}$ and a spatial extent of about 7.4 pc (∼7 core radii) in projection, and contains observations for some stars that extend back over 45 yr. Our orbital solutions span in orbital period from a few days out to a maximum orbital period of ∼14,000 days. We identify six triples in this sample. We present all orbit plots for SB1 and SB2 binaries and triples in Figures 1–3 with tabulated orbital parameters in Tables 2–4, respectively. All RVs for binaries, as well as single stars in our sample, are provided in Table 1. Although we focus our analysis in this paper on the main-sequence binaries, we also provide orbital solutions for red giants, yellow giants, and sub-subgiants (see the color–magnitude diagram in Figure 8 of Paper I for reference).

We analyze the main-sequence binary frequency and distributions of orbital parameters, correcting for observational incompleteness, and find the following results:

1. Within our mass and spatial domains, the M67 main-sequence stars have a binary frequency of $34\% \pm 3\%$ out to a period limit of 10^4 days. This binary frequency increases to $70\% \pm 17\%$ when we only consider the inner 0.4 core radii.
2. We find a circularization period for M67 of $11.0^{+1.1}_{-1.0}$ days by fitting a circularization function to the e-log P distribution of unevolved ($V > 13.5$) main-sequence binaries, in agreement with previous determinations.
3. The orbital period distribution rises toward longer periods, and is formally consistent with solar-type binaries in the field and in NGC 188. There is, however, an indication (at 2.81σ) that long-period binaries are missing compared to the field log-normal distribution, possibly due to dynamical hardening of the wider binaries by stellar encounters that drive them toward shorter periods. The period distribution is statistically inconsistent with a log-uniform distribution (at 3.96σ), a popular initial condition for binary population synthesis and star cluster models.
4. The eccentricity distribution for main-sequence binaries in M67 with periods between the circularization period and 3000 days is consistent with similar binaries in NGC 188 and the field, which can be described by a uniform distribution. A thermal distribution, which is popular in theoretical models, is ruled out at very high confidence (6.65σ).
5. The distribution of mass functions for the M67 binaries is consistent with a uniform mass-ratio distribution, but inconsistent with a distribution derived by drawing companions from an IMF (at 7.10σ). This result is consistent with solar-type binaries in NGC 188 and the galactic field.

These results focus on the main-sequence binary population, which dominates the mass of the cluster. They provide an important touchstone for star cluster dynamical models and more broadly, for studies of solar-type stars.

The authors would like to thank the many individuals who helped obtain these spectra, determine the stellar radial velocities, and solve for orbital solutions at the CfA: Jim Peters, Bob Davis, Ed Horine, Perry Berlind, Ale Milone, Robert Stefanik, Mike Calkins, Gil Esquerdo, Jessica Mink, and Christian Latham, and at the University of Wisconsin-Madison: Natalie Gosnell, Katelyn Milliman, Ben Tofflemire, and David Szymulewski. This research was made possible by the National Science Foundation grant AST-1714506 and the Wisconsin Alumni Research Foundation at the University of Wisconsin-Madison.

ORCID iDs

Aaron M. Geller https://orcid.org/0000-0002-3881-9332
Robert D. Mathieu https://orcid.org/0000-0002-7130-2757
David W. Latham https://orcid.org/0000-0001-9911-7388
Guillermo Torres https://orcid.org/0000-0002-5286-0251
Emily M. Leiner https://orcid.org/0000-0002-3944-8406

References

Ambartsumian, V. A. 1937, AZh, 14, 207
Belloni, T., Verbunt, F., & Mathieu, R. D. 1998, A&A, 339, 431
Davenport, J. R. A., & Sandquist, E. L. 2010, ApJ, 711, 559
Duchêne, G., & Kraus, A. 2013, ARA&A, 51, 269
Fan, X., Burstein, D., Chen, J.-S., et al. 1996, AJ, 112, 628
Geller, A. M., Hurley, J. R., & Mathieu, R. D. 2013, AJ, 145, 8

Geller, A. M., Latham, D. W., & Mathieu, R. D. 2015, AJ, 150, 97
Geller, A. M., Leigh, N. W. C., Giersz, M., Kremer, K., & Rasio, F. A. 2019, ApJ, 872, 165
Geller, A. M., & Mathieu, R. D. 2011, Natur, 478, 356
Geller, A. M., & Mathieu, R. D. 2012, AJ, 144, 54
Geller, A. M., Mathieu, R. D., Braden, E. K., et al. 2010, AJ, 139, 1383
Geller, A. M., Mathieu, R. D., Harris, H. C., & McClure, R. D. 2008, AJ, 135, 2264
Geller, A. M., Mathieu, R. D., Harris, H. C., & McClure, R. D. 2009, AJ, 137, 3743
Goldberg, D., Mazeh, T., Latham, D. W., et al. 2002, AJ, 124, 1132
Gosnell, N. M., Mathieu, R. D., Geller, A. M., et al. 2015, ApJ, 814, 163
Heggie, D. C. 1975, MNRAS, 173, 729
Hole, K. T., Geller, A. M., Mathieu, R. D., et al. 2009, AJ, 138, 159
Hurley, J. R., Pols, O. R., Aarseth, S. J., & Tout, C. A. 2005, MNRAS, 363, 293
Jeans, J. H. 1919, MNRAS, 79, 408
Kroupa, P. 2001, MNRAS, 322, 231
Kurtz, M. J., & Mink, D. J. 1998, PASP, 110, 934
Latham, D. W. 1992, in ASP Conf. Ser. 32, IAU Coll. 135, Complementary Approaches to Double and Multiple Star Research, ed. H. A. McAlister & W. I. Hartkopf (San Fransisco, CA: ASP), 110
Latham, D. W., Mathieu, R. D., Milone, A. A. E., & Davis, R. J. 1992, in Proc. IAU Symp. 151, Evolutionary Processes in Interacting Binary Stars, ed. Y. Kondo, R. F. Sistero, & R. S. Polidan (Dordrecht: Kluwer), 471
Latham, D. W., Stefanik, R. P., Torres, G., et al. 2002, AJ, 124, 1144
Leiner, E., Mathieu, R. D., Gosnell, N. M., & Geller, A. M. 2015, AJ, 150, 10
Leiner, E., Mathieu, R. D., Vanderburg, A., Gosnell, N. M., & Smith, J. C. 2019, ApJ, 881, 47
Leonard, P. J. T. 1989, AJ, 98, 217
Mathieu, R. D. 1983, PhD thesis, Univ. California, Berkeley
Mathieu, R. D. 1985, in Proc. IAU Symp. 113, Dynamics of Star Clusters, ed. J. Goodman & P. Hut (Dordrecht: Reidel), 427
Mathieu, R. D. 2000, in ASP Conf. Ser. 198, Stellar Clusters and Associations: Convection, Rotation, and Dynamos, ed. R. Pallavicini, G. Micela, & S. Sciortino (San Fransisco, CA: ASP), 517
Mathieu, R. D., & Latham, D. W. 1986, AJ, 92, 1364
Mathieu, R. D., Latham, D. W., & Griffin, R. F. 1990, AJ, 100, 1859
Mathieu, R. D., Latham, D. W., Griffin, R. F., & Gunn, J. E. 1986, AJ, 92, 1100
Mathieu, R. D., & Mazeh, T. 1988, ApJ, 326, 256
Mayor, M., & Mermilliod, J. C. 1984, in Proc. IAU Symp. 105, Observational Tests of the Stellar Evolution Theory, ed. A. Maeder & A. Renzini (Dordrecht: Reidel), 411
Mazeh, T., & Goldberg, D. 1992, ApJ, 394, 592
McCrea, W. H. 1964, MNRAS, 128, 147
Meibom, S., & Mathieu, R. D. 2005, ApJ, 620, 970
Milliman, K. E., Mathieu, R. D., Geller, A. M., et al. 2014, AJ, 148, 38
Milone, A. P., Piotto, G., Bedin, L. R., et al. 2012, A&A, 540, 16
Moe, M., & Di Stefano, R. 2017, ApJS, 230, 15
Montgomery, K. A., Marschall, L. A., & Janes, K. A. 1993, AJ, 106, 181
Nine, A. C., Milliman, K. E., Mathieu, R. D., et al. 2020, AJ, 160, 169
Perets, H. B., & Fabrycky, D. C. 2009, ApJ, 697, 1048
Raghavan, D., McAlister, H. A., Henry, T. J., et al. 2010, ApJS, 190, 1
Sanders, W. L. 1977, A&AS, 27, 89
Sarajedini, A., von Hippel, T., Kozhurina-Platais, V., & Demarque, P. 1999, AJ, 118, 2894
Tokovinin, A., Thomas, S., Sterzik, M., et al. 2006, A&A, 450, 681
VandenBerg, D. A., & Stetson, P. B. 2004, PASP, 116, 997
Yadav, R. K. S., Bedin, L. R., Piotto, G., et al. 2008, A&A, 484, 609
Zucker, S., & Mazeh, T. 1994, ApJ, 420, 806
Zucker, S., Torres, G., & Mazeh, T. 1995, ApJ, 452, 863